ABSTRACT

CHARACTERIZATION OF OPTICAL LATTICES USING PUMP-PROBE SPECTROSCOPY AND FLUORESCENCE IMAGING

by Ethan Clements

This thesis presents data from optical lattices using fluorescence imaging and pump-probe spectroscopy. From these experimental techniques we obtain information on the diffusion constant and vibrational frequencies of atoms confined in an optical lattice as a function of various lattice parameters. We see clear evidence of vibrational resonances which is a definite signature of optical lattices. These resonances are clearly distinguishable from Brillouin effects. We also discuss briefly our progress toward the measurement of photon correlations in light scattered by cold atoms.

CHARACTERIZATION OF OPTICAL LATTICES USING PUMP-PROBE SPECTROSCOPY AND FLUORESCENCE IMAGING

A Thesis

Submitted to the
Faculty of Miami University
in partial fulfillment of
the requirements for the degree of
Master of Science
Department of Physics
by
by Ethan Clements
Miami University
Oxford, Ohio
2016

Advisor ______________________

Dr. Samir Bali

Reader ______________________

Dr. James Clemens

Reader ______________________

Dr. Herbert Jaeger

TABLE OF CONTENTS

APPENDICES

LIST OF FIGURES

FIGURE PAGE

To my family, friends, and above all Avery
who have shown me so much love and support.

ACKNOWLEDGMENTS

I would first like to acknowledge my parents Allen and Dagmar who provided me with love and support which has made me very fortunate to be able to pursue my interests in science. Next I would like to thank Avery my fiance for helping me through these trials by supporting me with coffee and food as well as emotional support she truly is priceless to me. Next I would like to thank Samir Bali for his guidance and mentor-ship through both my undergraduate and graduate studies. I am forever grateful for the opportunities and lessons he has provided me. Next I would like to make a shout out to Preston and Tony who were excellent lab mates and friends I hope that I will be fortunate to encounter them both again in life and have the opportunity to grow together further. Big thanks is also necessary to the Miami University instrumentation lab particularly Mike Weeks and Jayson Alexander. They provided invaluable support at a moments notice and without them much of this thesis would have been impossible. And lastly I would like to thank my friends and especially Jeff Brock for the great memories and support through the years.

CHAPTER 1

INTRODUCTION

Manipulation and control of single atoms could lead to many breakthrough technologies and new research abilities. One place this is realized is through the use of optical lattices. Optical lattices were first realized in 1992 by Bill Phillips' group and were used to further cool atoms confined in a magneto optical trap (MOT). Optical lattices provide an ideal test bed for precise tunability and control of the environment for light-atom interaction. Because lattices offer such precise tunability the experimenter can study and control the dynamics of the confined atoms opening new opportunities to study condensed matter systems in incredibly pure environments (1). Many experimenters are currently using both lattices and Bose-Einstein Condensates (BEC) to study condensed matter systems such as the Bose-Hubbard model. This could lead to improvements in the techniques of nano-lithography which has many applications in data storage, nano-electronics, computation, and micro-fluidics.

Currently much of optical lattice work with BECs is being done in far detuned optical lattices to suppress the deleterious impact of spontaneous on the quantum coherence of the atomic wave-function. Because of the incredibly cold and dense nature of BECs one is usually able to ensure that each lattice site is occupied by at least one atom. We are constrained to dilute lattices with just one in a hundred sites actually occupied. However near-detuned dilute optical lattices still offer unique opportunities, such as the investigation of departures from Boltzman-Gibbs statistics (2; 3). Near-detuned (or"dissipative") dilute lattices are particulary amenable to measurement by fluorescence imaging and photon correlation techniques which would be nearly impossible to implement in far-detuned lattices. In this thesis we present our current progress toward implementing fluorescence imaging, pump-probe spectroscopy, and photon correlation methods for characterizing near-resonance optical lattices.

1.1 Thesis Organization

In Chapter 2 I describe our experimental setup. Next in Chapter 3, I introduce 1-D and 3-D optical lattices and describe our experimental procedure for alignment and studying diffusion in both lattice types lattice. I then provide the results from our 1-D and 3-D lattice diffusion study and discuss the results. In Chapter 4 I describe our study of vibrational resonances in lattices which we studied using pump probe spectroscopy. Chapter 5 is devoted to a recent apparatus design we developed for a dramatically more cost-effective infrared viewer. I then detail in chapter 6 our progress towards implementing photon correlation measurements in our optical lattice. Finally, in Chapter 7 I conclude by summarizing our results and provide a future outlook.

CHAPTER 2

EXPERIMENTAL SETUP

In this chapter we provide details of the various elements of our experimental setup that lay the foundation for our optical lattice experiments in ^{85}Rb.

2.1 Extended Cavity Diode Lasers

The lasers we use as the basis of our experimental setup are extended cavity laser diode systems in the Lithrow Configuration. We follow the design outlined by Wieman (4). To create this laser system we begin with a relatively broadband (few GHz) 785nm laser diode and narrow the frequency down to several tens of kHz or less. We do this by using a diffraction grating attached to a kinematic mount to steer the -1 order diffracted beam back in to the laser diode giving us a frequency narrowed and tunable laser system. We tune the laser by adjusting the angle of the diffraction grating to frequency tune the laser. We then use a servo-loop lock box which allows us to perform saturated absorption spectroscopy(SAS), and once the spectra are found, lock the laser frequency to one of these peaks.

The hyperfine transitions provide features that have power-broadened linewidths of $\sim$20MHz (natural linewidth for Rb: 6 MHz) that can be used to create a lock point. They are also of interest because they represent the hyperfine transitions used to laser-cool the atoms.

2.2 Tapered Amplifier (TA) Systems

We have sophisticated home-built tapered amplifier (TA) systems that provide us the laser power needed to perform optical lattice experiments.(5) After all of our alignments and frequency manipulations (see Figs 2.4 and 2.5), we are able to achieve 1-D lattice intensities of up to $15\,\mathrm{mW/cm^2}$ per beam and 3-D lattice intensities of up to $4\,\mathrm{mW/cm^2}$ per beam.

Some notes for future students:
If you leave your EDCLs ramping for too long you may occasionally induce current swings in the current controller of the TA system. So ideally when the TA systems are on the lasers should remain locked or have the ramp turned down as far as possible.When aligning through a fiber if you adjust the mirror right before the tapered amplifier you can slightly alter the mode profile of the laser entering the fiber, allowing you to optimize the mode profile to obtain the best coupling into the fiber.

2.3 Acousto Optic Modulators

In our lab we rely on acousto-optic modulators (AOM) for various purposes such as precise timing and frequency scanning. AOMs work by setting up a rf traveling wave of in a crystal that causes incident light to diffract in various orders (Please see Appendix A for a cautionary note regarding AO repair). Also because of the fact that this is a traveling wave it is unlikely that one should see any phase scrambling of the laser. To verify this fact, we divided the laser beam into two parts, and passed each part through an AOM. Each of these AOMs was driven by two output ports from the same RF oscillator, which were phase-locked with each other. This was checked using an interferometer and a detector to interfere the separately frequency shifted laser beams and measure their intensity beats as a function of their detuning from each other. Fig 2.1 shows a plot of the measured beat between the two AO outputs versus the theoretically expected beat. The excellent agreement suggests the phase relationship between the 2 AO outputs is preserved. The slope is .99 therefore demonstrating that the beat frequency as a function of detuning is only 1% off from the ideal value on average. Details of how the laser frequencies are controlled with the AOs used in our setup are provided in section 4.2.

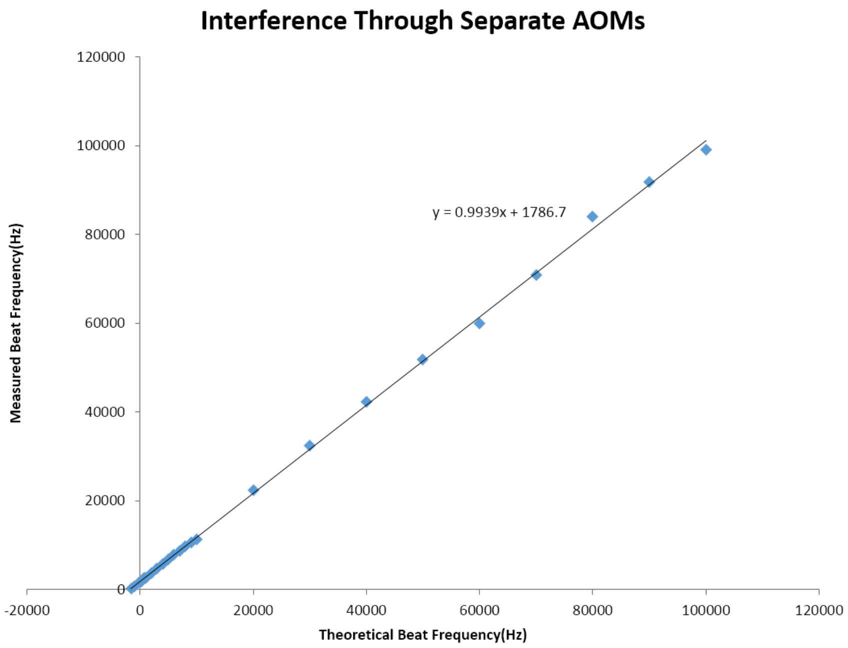

Figure 2.1: This figure displays the intensity beat from the interference of two beams passed through separate AOMs but derived from the same laser. The measured beat is plotted as a function of the theoretical beat.

2.4 Vacuum System

The major components of our vacuum system are a Kimball extended octagon with anti-reflection coated windows, and a Gamma Vacuum 20 L/s Ion pump. This system after having been properly cleaned and baked is able to achieve pressures as low as 1 nano-Torr. Two important notes for system operation and maintenance are provided below:

First there is a Mu-metal shield surrounding the high strength magnets on the ion pump. They only cover the top part of the ion pump because that is the only region thin enough to allow magnetic fields to permeate through.

Second, there is a need to maintain the turbo pump used to create a 1 microTorr vacuum before the ion pump can be switched on. Currently the pump is disconnected and turned off because the ion pump is a much stronger pump and is what maintains the vacuum in the cell. This is done to prevent pitting from stationary bearings, and the lubricant in the pump from dissociating. Every 4-6 months we must spin up the turbines of the turbo pump. To do this we have to first seal the section above the turbo with a section of vacuum pipe, a blank end seal, and a copper gasket. Then before turning on the turbo pump we first have to evacuate the system with the roughing pump. This is done by simply plugging the roughing pump in and waiting 20 minutes. Once the system is down to a few milli-Torr we can turn the turbo pump on and initiate the spin up sequence. For more details on how to operate the turbo pump see the blue colored manual attached to the turbo pump. To maintain the turbo pump it is only necessary to allow the turbo to spin for a few seconds. After it is allowed to spin you want to make sure to allow the pressure to re-normalize very slowly to standard atmospheric pressure to ensure that no oil from the roughing pump is sucked up into the turbo pump.

2.5 Doppler Cooling and Magneto-Optical Trapping

Doppler Cooling was a method proposed to cool the atoms in the low-velocity tail of the Maxwell-Boltzmann distribution even further down to micro-Kelvin temperatures. To implement Doppler cooling in one dimension you require two counter propagating laser beams that are detuned a few line-widths from the resonant frequency of atom. The transition we are detuning with respect to is the $5^2S_{1/2}F_g = 3 \rightarrow F_e = 4$ transition for ^{85}Rb. By having the lasers slightly detuned from the resonant frequency you can create a directional and velocity dependent force that is proportional to the velocity and in the opposite direction to the momentum vector of the atom. As an atom moves against the direction of laser propagation the relative motion of the atom with respect to the laser induces a Doppler-shift in frequency shifting it closer to the resonant frequency of the atom thus increasing the probability of the atom absorbing a photon. The photon absorbed by the atom gives the atom a momentum kick in the direction opposite to the direction of its momentum vector prior to the absorption. Subsequently, due to the atom experiencing spontaneous emission the net force experienced by the atom over time is always opposite to its direction of motion because when averaged over many absorption and emission events the net force of the spontaneous emission is zero. This effect is demonstrated in Fig. 2.2. This method cools many atoms to micro Kelvin temperatures but leaves them distributed over a large region(approximately the beam overlap volume) with a dilute density.

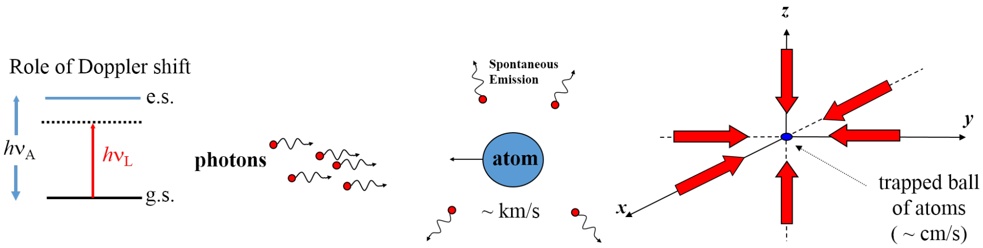

Figure 2.2: This figure details the purpose of detuning our lasers in order perform Doppler cooling of the atoms. The motion of the atom causes the energy levels to be light shifted and absorbing the photons and then spontaneously emitting the photons in a random direction thus cooling the atom

A spatial magnetic gradient of about 10G/cm is used to take the now cooled atoms and create a spatially dependent force that influences the atoms to congregate in a smaller region of about $1 - 3\text{mm}^3$. A figure to aid in this explaination can be seen in Fig. 2.3. This creates a standard workhorse magneto-optical trap (MOT)

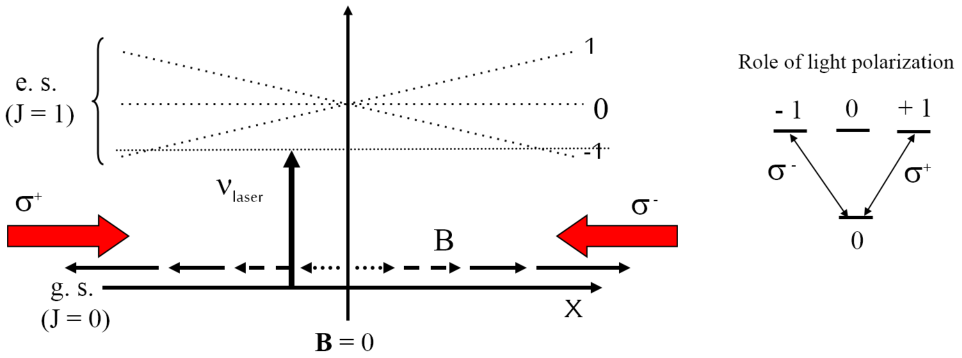

Figure 2.3: The B-Gradient causes a spatially dependent shift of the magnetic sub-levels creating a minima at the center of the chamber where B=0

2.6 Experimental Layout

In figure 2.4 we have three main sections the lattice(pump) setup, the imaging beam setup, and the probe beam setup. To begin, the output of our laser source is passed through an optical isolator(OI) to prevent back reflections into our laser which can cause instabilities in our saturated absorption spectroscopy. The laser then goes into a tapered amplifier (TA) amplifying the power by a factor 20. The laser is then sent through another OI to prevent back reflections from entering the output of the TA which could cause irreversible damage. The beam is then sent into an Acousto-Optic Modulator (AOM1) which give an initial negative shift in frequency. The laser then passes into a polarizing beam splitter (PBS) one component being split again supplying a laser to both the imaging beam setup and the probe beam setup. The half-wave plates ($\lambda/2$) before each PBS is what controls the percentage of the laser through each of the setups. The laser that continues to propagate in the lattice setup passes through AOM2 which gives a positive frequency shift which will provide the final frequency of the lattice beams. For the probe setup we require a double pass to provide the same final frequency that AOM2 provides and to prevent the position of the laser from changing as we scan the probe beam from pump-probe spectroscopy.

It this then injected into the fiber and sent to the other table. The imaging setup requires a double pass in order to achieve a large enough frequency shift to put it close enough to resonance to provide sufficient signal for fluorescence imaging.

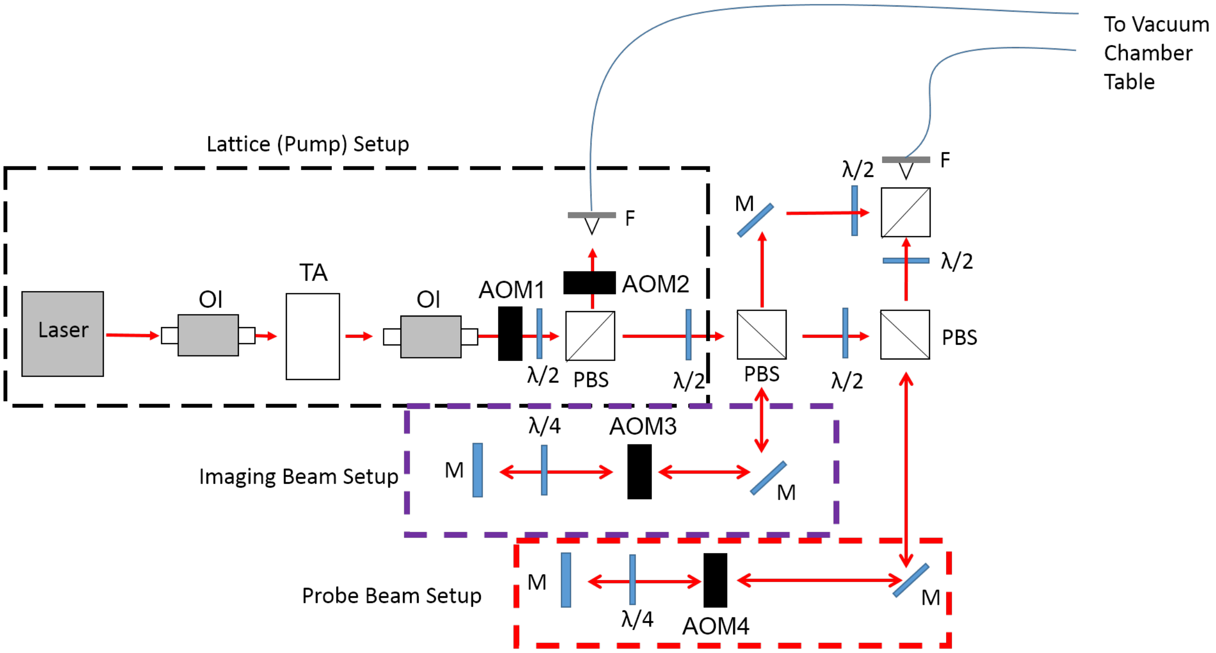

Figure 2.4: This is the experimental setup that is used to adjust the power and frequency of the lattice, probe, and imaging beams in the setup. OI(Optical Isolator), TA(Tapered Amplifier), AOM(Acousto-Optic Modulator), PBS(Polarizing Beam Splitter), F(Fiber)

The second half of our setup still has the same three sections as seen in Fig. 2.5. To begin we have two lattice beam outputs due to the intensity being split between two beams by a fiber splitter. The outputs of these fibers then pass into beam expanders to expand the beams from 2mm to 2cm. They are then sent through 1cm pinholes to cut the edges of the laser profile in order to produce flat top distributions. These beams can then be directed to be either 1-D or 3-D beams using a half-wave plate. The 1-D path is denoted by following the laser passing through P1 and P2. The probe and fluorescence beams come out of a fiber and depending on if you want the fluorescence beam or the probe beam you rotate the half-wave plate maxing intensity through beam expander for the fluorescence beam and up to the mirror for the probe. the only detail left is the quarter-wave plate ($\lambda/4$) present in the beam path. By converting the polarization to circular you require less intense beams to fluoresce the atoms.

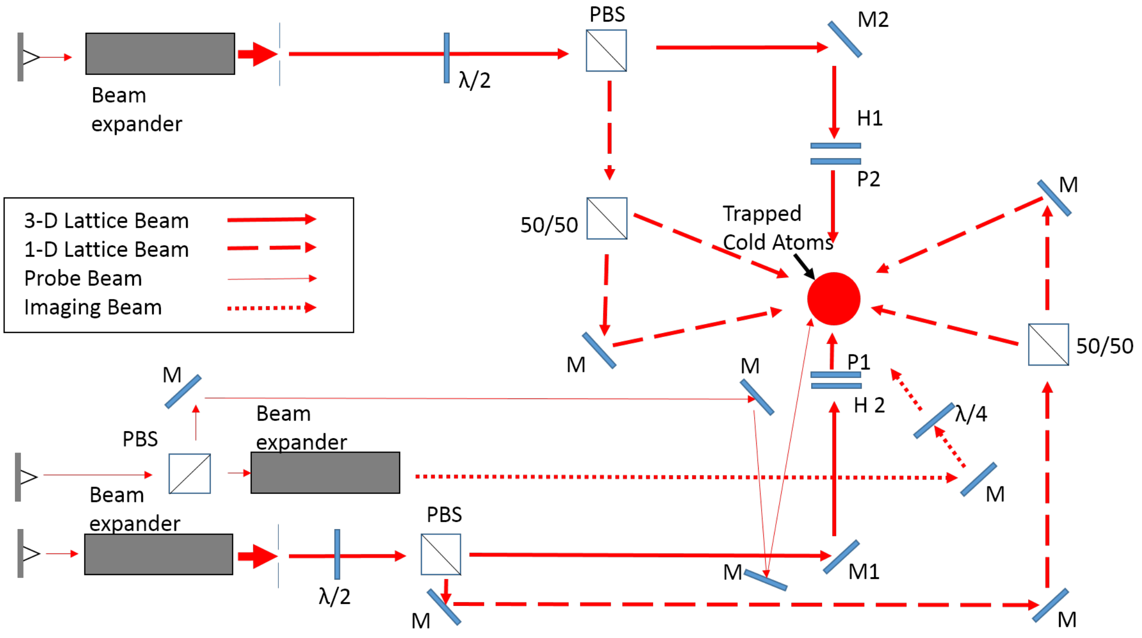

Figure 2.5: This is the extended experimental setup that details the general layout of the lasers that are used for the lattice, the probe, and the fluorescence beam

Following these setups all of the infrastructure should be in place to effectively perform 1-D and 3-D optical lattice experiments. While some details may be lacking, the main structure of these setups should give you enough of an idea of how the different orientations are necessary for optical lattice experiments.

CHAPTER 3

MEASUREMENT OF DIFFUSION CONSTANT IN 1-D AND 3-D OPTICAL LATTICES

In this chapter we provide background for 1-D and 3-D optical lattices, detail our method for obtaining diffusion constants, and provide our results. We see close agreement within an order of magnitude to prior work done by Schiavoni (6) as well as some interesting trends as intensity and detuning are changed.

3.1 Fluorescence Imaging With Fast Homebuilt Camera

We now have a state-of-the-art fast imaging camera system (7). We use this new camera system to image the expansion of the cold atom cloud confined in the optical lattice Figure 3.1 shows the camera and 4f imaging setup employed. The diffusion constant is extracted by taking snapshots of the cloud as it diffuses through the lattice and then measuring the FWHM of the fluorescent image as a function of time.

One issue we encounter when working with the camera system is that there is inherent jitter when the camera takes a picture. One can reduce the effects of jitter with an independent imaging beam that is pulsed at a much more consistent time than the initiation of the camera exposure. This is because the camera exposure timing is sourced from a TTL system while the light pulse is created by an AOM. By creating a longer camera exposure time that jitters around but always encompasses the imaging pulse we can effectively cut back on the error due to the inherent jitter of the camera pulse. The background light is minimal due to the lattice beams being

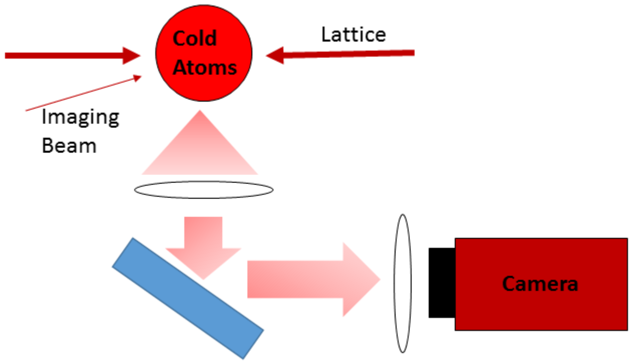

Figure 3.1: The setup we use to do fluorescence imaging with our camera system. We use a 4-f lens system that employs two inch f = 170mm lenses and a two inch dielectric mirror.

detuned by several line-widths but the background can always be removed by first taking a background image while blocking the imaging beam and then subtracting the background from the image of the data. By following this method one can reduce the uncertainty in the instant at which the camera took the picture to ±0.5 ms (7). We studied the jitter by varying the time duration for which a laser beam is incident on our camera. Our camera had a set exposure length so when the laser-on time was much longer than the camera exposure time ± the jitter, the camera would have a set number of counts. As the laser-on time is reduced the exposure time moves outside of the time the laser is on, decreasing the average number of counts. This allowed us to quantify our jitter. By switching roles and having a set laser-on time instead, while decreasing the camera exposure time we could quantitatively identify the regime where jitter causes the least change to our data. The results are seen in Fig. 3.2.

By using an independent imaging beam we can ensure a timing certainty within 0.5 ms of when our image was taken. This reduction of jitter allows us to cut back on our uncertainty and variance thus giving us a reduction in our standard deviation.

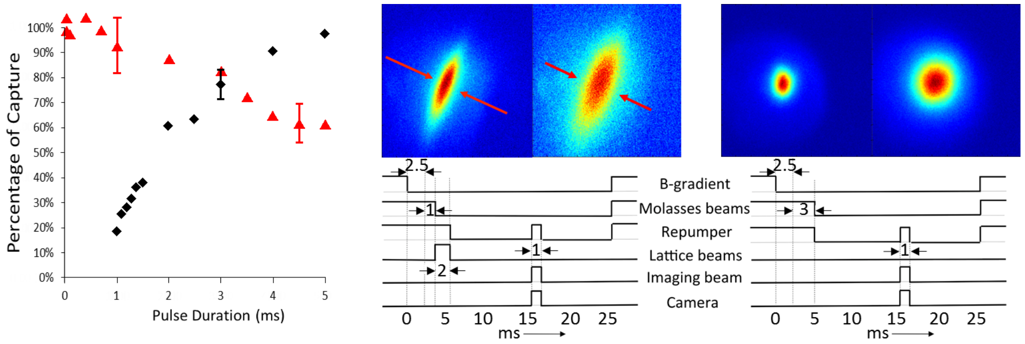

(a) (b) (c)

Figure 3.2: Reproduced from Ref.[8] (a)Measurement of a jitter of 2 ms in camera exposure time(black diamonds) and a demonstration of precisely timed 1 ms snapshots (red triangles). Representative error bars, derived from 30 measurements, are shown for some datapoints. (b) and(c) show snapshots at t = 2 ms (left) and 6 ms (right) of the ballistically expanding sample initially confined in (b) a 1D lattice or (c) molasses. The two thin arrows in (b) indicate the counter-propagating 1D lattice beams. Representative timing diagrams are included just below the snapshots.

The error in our data can be further reduced by imaging at a set time and averaging over many exposures. The error follows this function

$\frac{\sigma}{\sqrt{\mathbf{n}}}$ where σ is the standard deviation and n is the number of exposures

By using the independent imaging beam to reduce our standard deviation and imaging over about 100 exposures we obtain errors on the order of a percent giving us enough timing certainty to feel comfortable studying atomic dynamics in an optical lattice.

3.2 Lattice Alignment

3.2.1 1-D Lattice

In order to set up the 1-D Lattice we first inject the laser into a fiber splitter. This allows the beam to be split in fairly equal intensities of about 40/60 out of the two output ports of the fiber, which are then counter propagated with respect to each other to form the 1-D optical lattice. The procedure is as follows:

• First remove the polarizers (P1 and P2) directly before the chamber seen in Fig. 2.5 or align them to be the same polarization to prevent the counter propagating lasers from being attenuated.

• Next using M1 and the mirror right before align the first beam through the windows by centering them on the windows and making sure that the laser height doesn't sink over distance when passing through the two windows. The mirror just before is not labeled but in order to walk a laser you require 2 mirrors.

• Make sure that the beam is intersecting with the MOT by ensuring that you see a maximum disturbance of the cold atom cloud from the lattice laser for weakest possible intensity.

• Now align the second beam by making it co-linear to the first. This is done by first using mirror M2. Next use the mirror just before M1 to align the originally aligned beam through the pinhole on the other side of the chamber. Rinse and repeat until you see fluorescence in the fibers.

• Continue doing this until you maximize the fluorescence seen in both fibers.

• Now set the polarizers P1 and P2 in Fig. 2.5 by turning one to minimize the intensity of the counter-propagating beam passing through it.

• Finally set the intensities entering the chamber by turning the half-wave plates H1 and H2 from Fig. 2.5 to adjust the intensities passing through the corresponding polarizers.

It is important to note that if your lattice beam diameter is larger you can obtain better lattices because the atoms are now bathed in light which is larger than the size of the MOT that they are loaded from. (8) The smaller the beams intersecting, the less atoms are loaded into the trap, yielding small signals when imaging. We began by setting the beams at 6mm but later increased them to 1cm. This was purely for convenience because we decided to use 1cm beams for the 3-D lattice and this made switching between the 1-D and 3-D lattices easier.

In order to reduce uncertainty in the characteristics of our lattice it helps to create a beam that has a top-hat spatial intensity profile. While not a perfect top-hat one can get pretty close by first expanding the beam much larger than the final size of the beam and inserting a pin hole to cut out the desired size beam from the much larger beam. Currently we expand the beam to twice the radius of the final beam radius but in the future there may be an interest in making the initially expanded size small in order to increase the final intensity of the beam.

After proper alignment we see 1-D lattice lifetimes of about 30ms which are adequate to study the rate of expansion of the lattice and from this extract the diffusion coefficients.

3.2.2 3-D Lattice

To begin aligning the 3-D lattice we start by closing the apertures down to about a half a centimeter. We then place the window caps on our chamber which have paper strips taped to them which. For the vertical alignment the edges needing to be aligned correspond with the top edge for the top beam and the bottom edge for the bottom beam and for horizontal alignment they should be centered on the paper strip and one should see the top half of the beam on the cap. Using normal laser walking to place the beams on the marked spots on either side of the chamber one should be roughly aligned to have a lattice with a $\theta_x = \theta_y = 25^\circ$.(see Fig. 3.7)

The next step is to close the apertures down to as tight as they go ($\sim$2mm), unlock the lattice laser to let it frequency scan, and check that each beam is independently perturbing the MOT. The alignment of the lasers should be adjusted slightly to obtain the biggest perturbation on the trapped atoms.

Lastly one should lock the lattice lasers and begin imaging with the MOT B-fields turned off. Make sure the lattice is always on during this process. By playing with the exposure time of the camera and blocking all the beams except one at a time you should see the laser florescence the background vapor. This allows us to even more precisely align the lasers to overlap the MOT cloud. By performing this alignment procedure one should obtain 3D optical lattice lifetimes of ∼1 second, comparable to molasses lifetimes.

3.3 Extracting the Diffusion Constant from the Flourescent Camera Images

In this section we detail our method for extracting the diffusion constant from the time varying exposures. Making the assumption that the diffusion is Brownian we can treat the shape of the fluorescence image as Gaussian. For the equation of a Gaussian centered about zero we have

$$f(x) = ae^{-\frac{x^2}{2\sigma^2}} \tag{3.1a}$$

where in this case $x = \pm\sigma\sqrt{2ln(2)}$ are the FWHM points on either side of the Gaussian. The diffusion constant D is defined as $2D \equiv \frac{d}{dt}\langle x^2\rangle$ where $\langle x^2\rangle = \sigma^2$ specifies the mean square width of the cloud in the x-direction. (6). The relationship between the expanding FWHM of the cloud and the diffusion constant is straightforwardly found as follows:

$$FWHM = 2\sigma\sqrt{2ln(2)} = 2\sqrt{\langle x^2\rangle}\sqrt{2\,ln2} \tag{3.2a}$$

$$\Rightarrow \langle x^2\rangle = \frac{FWHM^2}{8\,ln2} \tag{3.2b}$$

$$D = \frac{1}{2}\frac{d}{dt}\langle x^2\rangle = \frac{1}{16\,ln2}\frac{\delta(FWHM^2)}{\delta t} \tag{3.2c}$$

3.3.1 Diffusion Constant for the 1-D Optical Lattice

The simplest form of an optical lattice , as shown in Fig. 3.3 is a 1-D optical lattice. Most would consider the periodic array to be formed by using intensity wells. However the method we chose to follow is to create an anti-ferromagnetic lattice by inducing spatially periodic light-shifts that are created using polarization gradients. For the case of the 1-D lattice this is done by forming a superposition of two collinear frequency-matched lasers with orthogonal linear polarizations, known as "Lin⊥Lin configuration". An equation for the spatial structure of the electric field can be solved by creating a superposition of the electric fields $\mathbf{e_x} E_0 e^{i(kz-\omega t)}$, and $\mathbf{e_y} E_0 e^{i(kz-\omega t)}$ with crossed polarizations, yielding a polarization gradient with a spatial periodicity of $\lambda/2$, as shown in fig. 3.3

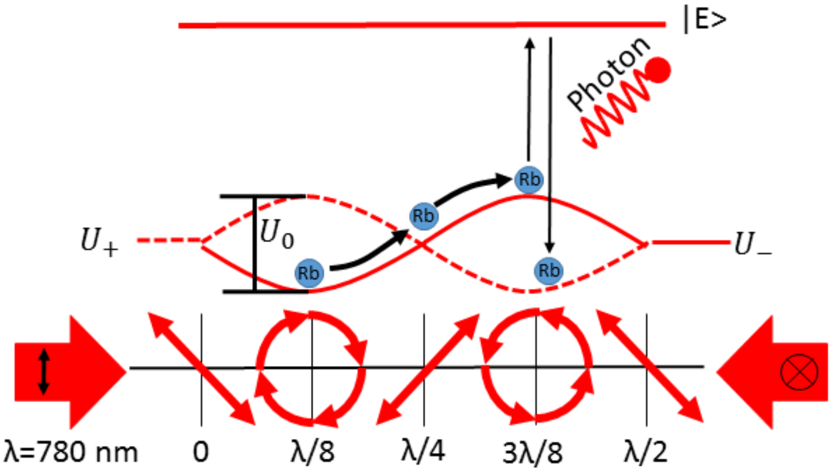

Figure 3.3: This figure illustrates the polarization gradient that is created by the superposition of two counter propagating laser beams of similar frequency and orthogonal polarizations. Here you can see the two light shifted energy levels U_+ and U_- which is what controls the motion of the atom in the lattice. Here the x-axis is vertical, while the y-axis points out of the page.

By frequency tuning the lasers using an acousto-optic modulator(AOM), and adjusting the intensity of the laser beams using a half-wave plate/polarizer combination, one may adjust the lattice potential thereby controlling the strength of the Sisyphus Cooling in the lattice.

To begin the process for measuring the diffusion constant we first measure the full width half max (FWHM) of each exposure and then calculate standard deviations

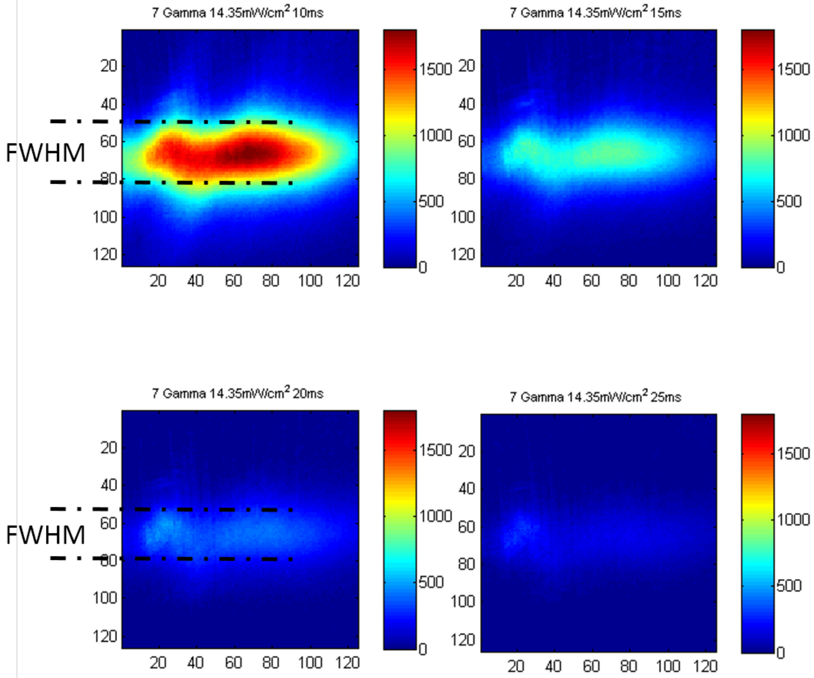

Figure 3.4: Exposures taken at 5ms time intervals are shown above to illustrate the change in the FWHM from image to image denoted by the dotted lines. The figure also demonstrates how you would expect atoms to diffuse in a 1-D lattice. They move much slower along the axis of the lattice which in this cae is the z axis and move ballistically in the other directions seen along the x axis. The intensity displayed here is the intensity of a single lattice beam

and average over 100 exposures to obtain the FWHM value of data. We do this by operation by running a fairly simple MAT-lab code detailed in Appendix B. After running this program we obtain an array of FWHM data points for each exposure taken. We then average and calculate the standard deviation for all of the values, convert from units of pixels to cm, and square the FWHM. The conversion from pixels to cm was calculated by moving the lattice beam close to resonance and imaging the fluorescence created from the background vapor. With this image we can use the known size of the beam (which in this case is 2mm) and measure the pixel width between the two steep count plateaus. This gives us a conversion factor of $5.2 \times 10^{-3} \frac{cm}{pixel}$. The images we use to obtain the FWHMs from which are then used to obtain our data on diffusion constants is displayed in Fig. 3.4. The slope we obtain from plotting these FWHM is linear and is within an order of magnitude with data taken by the Phillips group (9). We currently measure 1-D diffusion constants in the vicinity of .02 cm^2/s. There is no clear trend present for how the diffusion constant varies with intensity and detuning but we do see that we are within an order of magnitude from what is expected. Currently we are seeing a negative diffusion constant for some graphs. We think the negative values could be caused by the atoms leaving the region to quickly in the directions not confined by our optical lattice causing the max of our FWHM to decrease to quickly in relation to our full width.

3.3.2 3-D Optical Lattice

The process for making a 3-D lattice is very similar to the method of making a 1-D lattice. Again the intersecting lasers are arranged in the Lin⊥Lin configuration so there is a periodic interference pattern like that of the 1-D lattice. However, because we now require there to be a 3 dimensional periodicity we must intersect a minimum of 4 lasers to achieve a 3-D structure (10). The configuration of the lasers follow Fig. 3.5

Again this structure follows from the superposition of the electric fields of the four laser beams, the final results for which are written in Eqn.5 below:

$$E(z) = Re[(E_+\mathbf{e}_+ + E_-\mathbf{e}_-)e^{-i\omega t}] \tag{3.3a}$$

$$E_\pm = \sqrt{2}E_0 e^{ik_- z} \cdot [\cos(k\sin\theta_x x)e^{ik_+ z} \mp \cos(k\sin\theta_y y)e^{-ik_+ x}] \tag{3.3b}$$

$$\text{where} \quad k_\pm = \frac{k(\cos\theta_x \pm \cos\theta_y)}{2} \tag{3.3c}$$

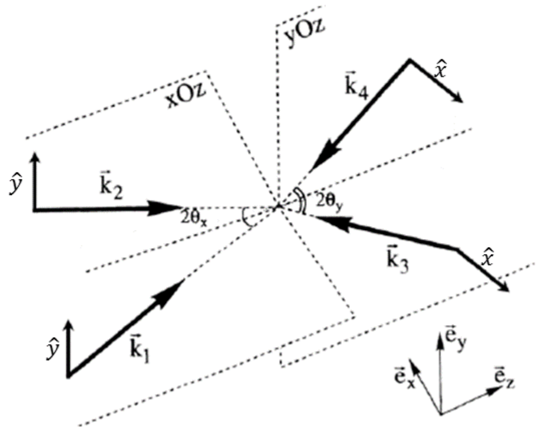

Figure 3.5: Here we see the arrangement of four laser beams used to create a 3-D optical lattice where the k's are the wave vectors of the four intesecting laser beams and 2θ is the angle between laser beams. In our experiments, $\theta_x = \theta_y$.

The three dimensional potential is now given by

$$U_{\pm}(x,y,z) = U_0[(3k^2\sin^2\theta_x)x^2 + (3k^2\sin^2\theta_y)y^2 + k^2(\cos\theta_X + \cos\theta_y)^2z^2] \tag{3.4}$$

where U_0 is the depth of the 1D bi-potential well for the 1D lattice and is given by (11)

$$U_0 = \frac{\hbar\Gamma}{2}(\frac{\Delta}{\Gamma} - \sqrt{\frac{\Delta^2}{\Gamma^2} + \frac{I}{2I_0}}) \tag{3.5}$$

Due to the imaging process being identical to the 1-D case I will include the figures obtained but will not go into detail the process for obtaining them. We again display the images that are used to determine the FWHM in Fig. 3.6.

We now take the FWHMs obtained from these images convert them into σ^2 and plot them vs. time to obtain the diffusion constant.

The slope of the graph in Fig. 3.7 provides the diffusion constant and is our method for obtaining the diffusion constant for other intensities and detunings. After doing this for our other sets of detunings and intensities we obtain Figs. 3.8 - 3.11.

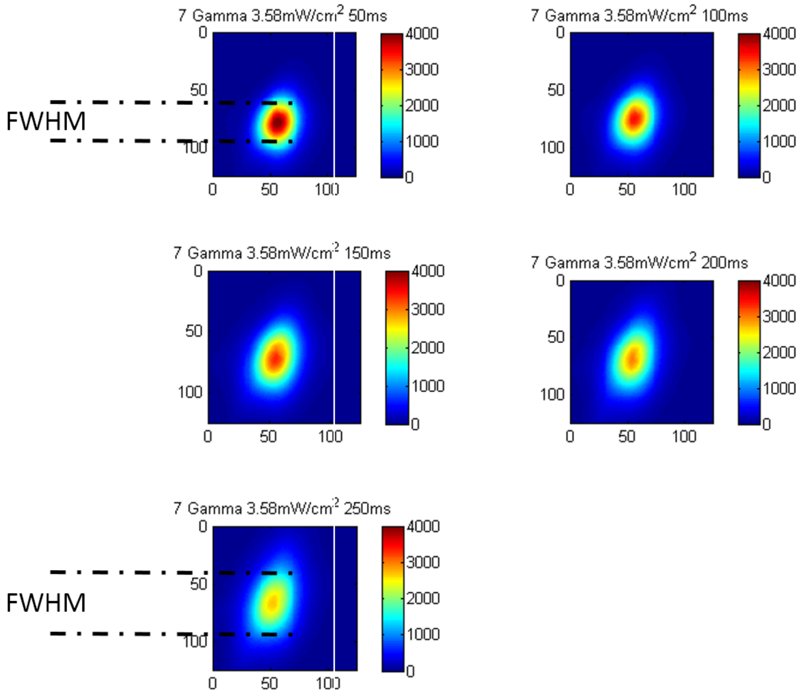

Figure 3.6: Exposures taken at 50ms time intervals are shown above to illustrate the change in the FWHM from image to image denoted by the dotted lines. The figure also demonstrates how you would expect atoms to diffuse in a 3-D lattice. The intensity displayed here is the intensity of a single lattice beam

In Fig. 3.8 we don't see a clear trend from the change in detuning but what we can see is that we remain below a diffusion constant of .05 cm^2/s. Comparing our result to work done by Schiavoni (6) we find we always remain in agreement within a factor 10. We avoid comparing our results to theory and restrict ourselves to comparing with prior experimental data by other groups because when comparing it to a theoretical model presented by Phillips (9) we find our data lies in a regime outside the validity range of the theory.

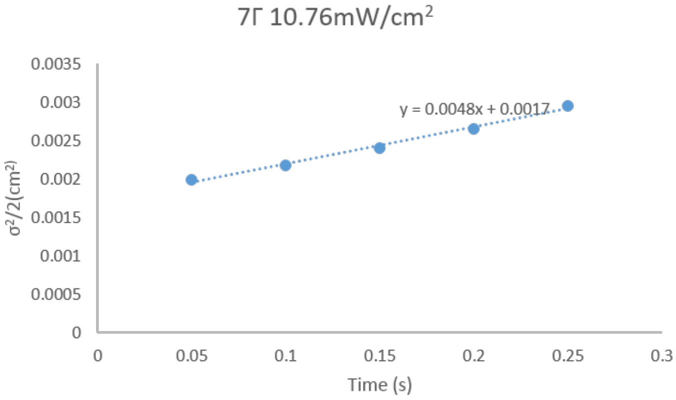

Figure 3.7: Here we see the expected linear trend of σ^2 as a function of time. The intensity displayed here is the intensity of all lattice beams

$$\text{Ref[1] says that} D \cong \frac{1}{3}\frac{\Gamma}{k^2}(\frac{\Gamma}{\Delta})^2\frac{I}{I_0} \tag{3.6a}$$

$$\text{provided the criterion } (\frac{|\Delta|}{\Gamma})^{3/2} \ll 12(\frac{I}{I_0})^{1/2} \text{ is satisfied} \tag{3.6b}$$

In our case the inequality (3.6b)is not satisfied at all, when inserting values into equation 3.6a that correspond to our experimental data we see a two order of magnitude difference. We are not close to fulfilling the validity condition and because of this we chose to compare our data to experimental results by others such as (6) and (12).

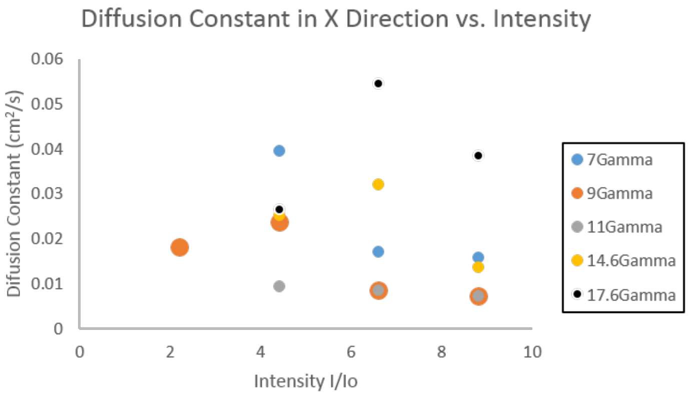

Figure 3.8: This graph displays the diffusion constant in the x direction vs. intensity for 5 detunings. The intensity displayed here is the intensity of all lattice beams

In Fig. 3.9 we see the trend of the diffusion constants plotted as a function of Intensity. Here we can see that in this regime of detunings the effect of changing the intensity creates a parabolic trend with the low point existing around 7 I/I_0

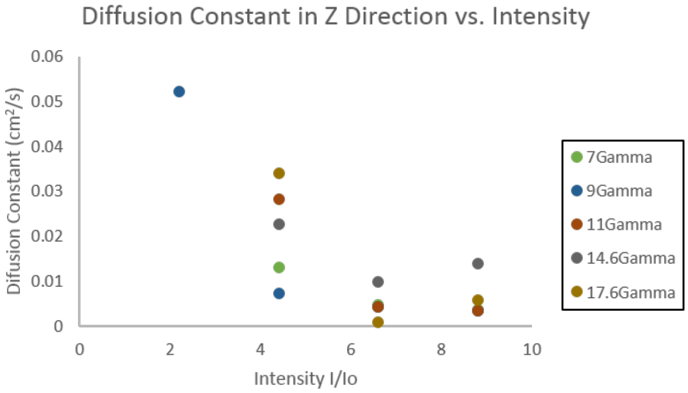

Figure 3.9: This graph displays the diffusion constant in the z direction vs. intensity for 5 detunings. The intensity displayed here is the intensity of all lattice beams

In Fig. 3.10 much like the prior graph we see the trend of the diffusion constants plotted as a function of detuning. Here we can see that in this regime of intensities the effect of changing the detunings creates a parabolic trend with the low point existing around 11 Γ

In Fig. 3.11 we see the trend of the diffusion constants plotted as a function of detuning. We see that as we move close to lower intensities the trend of the diffusion constant increases.

Overall we can conclude from these graphs that we are able to obtain variations in the diffusion coefficient as we change intensity and detuning but most importantly the data we are obtaining is within an order of magnitude from what others have done in past work(6; 12).

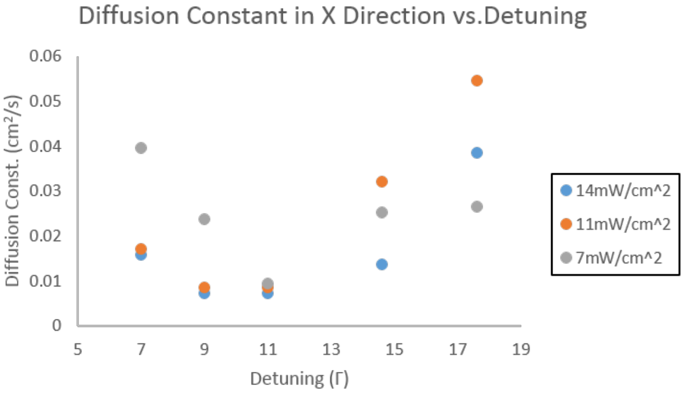

Figure 3.10: This graph displays the diffusion constant in the x direction vs. detuning for 3 sets intensities. The intensity displayed here is the intensity of all lattice beams

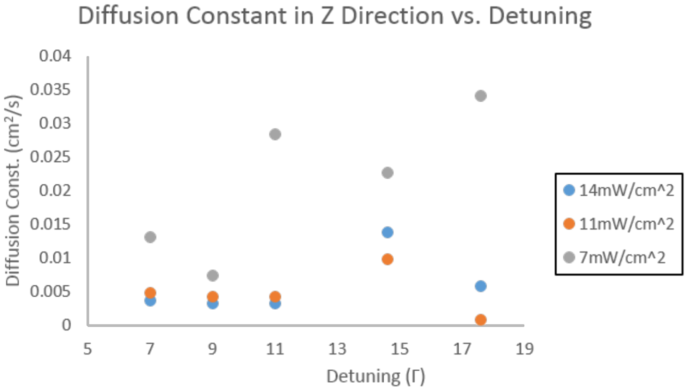

Figure 3.11: This graph displays the diffusion constant in the z direction vs. detuning for 3 sets intensities. The intensity displayed here is the intensity of all lattice beams

CHAPTER 4

PUMP-PROBE SPECTROSCOPY OF VIBRATIONAL ENERGY LEVELS IN 3-D LATTICES

In this chapter we lay out our process for performing pump probe spectroscopy to study the vibrational resonances of our 3-D optical lattice. We also present our data on vibrational and Brillouin resonances and their close agreement to a theoretical model.

4.1 Pump-Probe Spectroscopy: Concept

Now turning our focus to another characteristic of the potential wells we can see due to the wells of the lattice being very similar in nature to the potential of a harmonic oscillator one would expect to see vibrational resonances. The vibrational frequencies in the x and y directions of the 3D lattice in Fig. 3.5 are given by (10)

$$\Omega_{x,y} = \frac{\sqrt{3U_0 E_{Rx,y}}}{\hbar} \tag{4.1a}$$

$$\tag{4.1b}$$

where $E_{Rx,y}$ is the recoil energy given by

$$E_{Rx,y} = \frac{\hbar^2 K_{x,y}^2}{2M} \tag{4.2}$$

Here M is the Atomic mass $K_{x,y} = \frac{2\pi}{\lambda}\sin\theta_{x,y}$ and U_0 is defined in equation 3.5. A specified lattice vibrational frequency is achieved by varying the laser detuning or by adjusting the intensity of the lattice beams. The detuning δ is defined as

$\omega_{probe} - \omega_{pump}$. Using such “knobs” we will finely control and study the vibrational levels as a function of electric field strength and laser detuning.

The method used to study these effects is pump-probe spectroscopy. Pump-probe spectroscopy is the process of scanning the frequency of a probe laser around the fixed frequency of a pump beam to observe characteristic spectral features in the probe transmission spectrum, as shown in Fig. 4.1

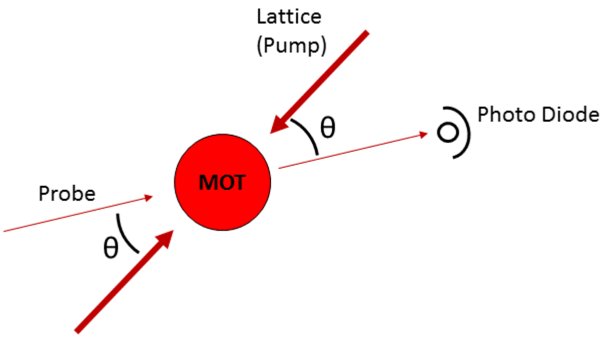

Figure 4.1: The probe beam intersects the lattice at a small measured angle and is frequency scanned about the pump beam.The transmission spectrum of the probe beam is then measured to determine the vibrational frequency of the lattice. Note that in our experiments we chose to scan the pump instead of the prob. The scans are small enough that the pump beams (which are actually the lattice beams in our case) do not affect the lattice significantly

Due to the weaker confinement of atoms in 1-D lattices compared to 3-D we chose to skip 1-D expecting the probe transmission spectrum for the 3-D lattice to be much less difficult to see. Also due to the confinement in all three dimensions the lifetime of the molasses in the lattice should be greater than in the 1-D case because atoms won’t be able to easily escape in directions where there is no confinement. This should also increase the signal we receive over the course of data collection.For a 3-D structure we have three separate angle dependent vibrational frequencies (10). We can selectively pick which vibrational frequency we excite by controlling the direction of the probe beam with respect to the lattice.

4.2 Pump-Probe Spectroscopy: Implementation

Following (6) we perform pump probe spectroscopy of a 3-D lattice using the lattice beams as a pump and a separate weak beam derived from the lattice beam as the probe. Following intersection with the cold atom sample, the probe beam is incident on a photo-diode which allows us to measure the transmission of the probe through the lattice as we scan the probe frequency. The probe beam needs to be double passed through an AOM before entering the chamber to give us enhanced frequency scanning ability as well as preventing any spatial shifts, which cause misalignments in the laser beam. The laser beams are directed to the cold atoms via single mode optical fibers, so any angular deflection of the laser beam at the AOM will cause a misalignment resulting in reduction of the fiber throughput. This intensity fluctuation would cause systematic error in the measurement of the vibrational frequencies of the lattice. The frequencies of all the beams in our setup are shown in Fig. 4.2

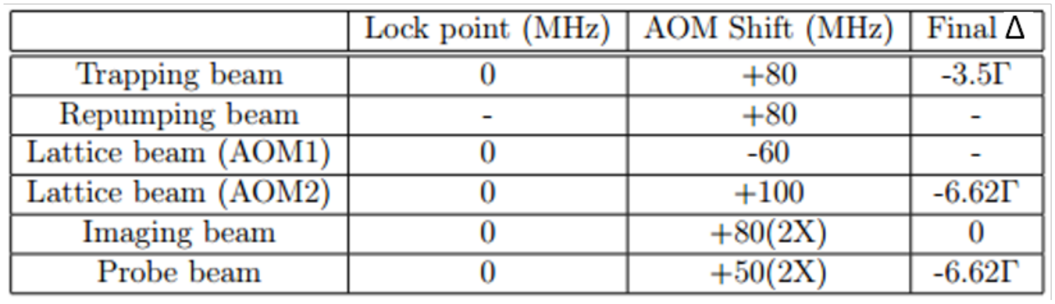

	Lock point (MHz)	AOM Shift (MHz)	Final Δ
Trapping beam	0	+80	-3.5Γ
Repumping beam	-	+80	-
Lattice beam (AOM1)	0	-60	-
Lattice beam (AOM2)	0	+100	-6.62Γ
Imaging beam	0	+80(2X)	0
Probe beam	0	+50(2X)	-6.62Γ

Figure 4.2: Table describing the frequency shifts of the AOMs in our setup and their final net detuning. The frequency shifts of AOM 1 do vary throughout the pump-probe spectroscopy experiment as we change parameters but the frequency shift is always negative. Here Δ is the detuning from atomic resonance

A typical experimental plot of the probe transmission spectrum, for a lattice detuning of -8.6 Γ and a lattice beam intensity (per beam) of 3.6 mW/cm^2, is depicted in Fig. 4.3. In our experiments, the probe beam is held fixed in frequency while the pump is scanned around the probe at a rate of 3 MHz/60 ms. When obtaining images such as depicted in Fig. 4.3 we averaged over 20 shots.

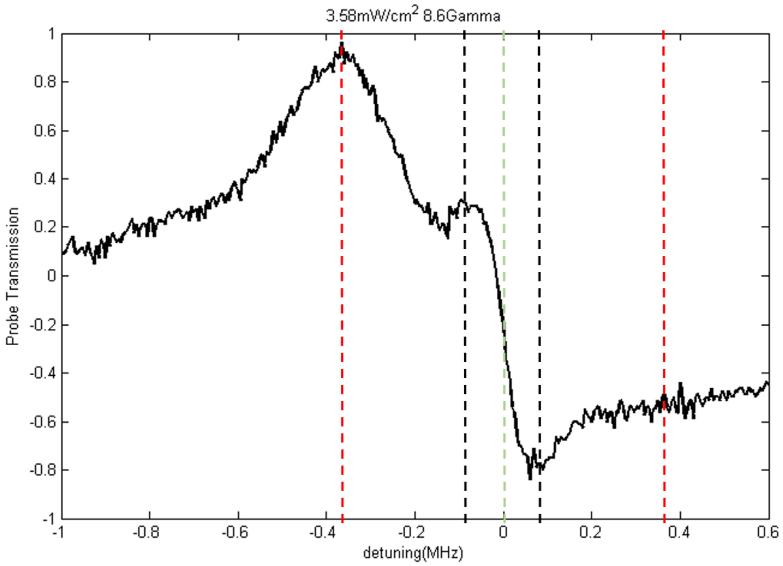

Figure 4.3: This experimental probe transmission spectrum illustrates the features we see when performing pump probe spectroscopy on atoms confined in the optical lattice with a probe beam polarized along the y-axis. The vibrational frequency is given by the location of the enhanced transmission peak or absorption dip. The dashed red lines demarcate the vibrational frequency. The black lines likely indicate Brillouin resonances as they are less sensitive to intensity and detuning changes. The Green dashed line indicates the midpoint between the Brillouin peak and dip- we use this as the counterpoint for our spectra, denoting this as the point where pump-probe detuning is zero. Here the intensity per beam is 3.58 mW/cm^2.

Interesting peaks and dips are observed in Fig. 4.3. As discussed in Sec. 4.3, the vertical red dashed lines locate the vibrational frequency for the atom oscillating inside the potential wells. Fig. 4.4 explains how the vibrational frequency gives rise to a peak and dip in the probe transmission spectrum. The figure shows the quantized vibrational energy- level structure in each potential well. The vibrational frequency is just the separation between the vibrational energy levels. For the case of enhancement of transmission, the pump beam excites the atom and the probe beam causes stimulated emission thus giving an enhancement in the intensity of the probe. For the case of the decrease in transmission, the probe beam excites the atom and then the pump causes stimulated emission giving rise to a decrease in the intensity of the probe beam (i.e.,dip)

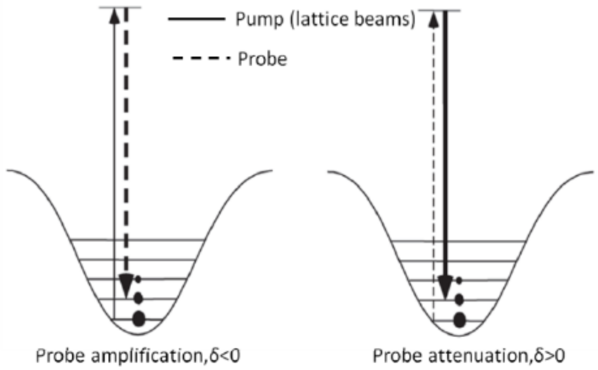

Figure 4.4: Origin of peak and dip in probe transmission spectrum shown in 4.3 For δ <0.

Following Fig. 4.4 the pump beam acts as the excitation laser and the probe causes stimulated emission giving rise to an enhancement in transmission. For δ >0 the probe acts as the excitation laser and the pump causes stimulated emission leading to a loss of a photon from the probe beam or an effective absorption. The size of the black dots represent the population of atoms occupying a vibrational energy level. δ is the detuning of the probe beam from the pump beam (recall that the pump beam is represented by the lattice beams).

The vertical black dashed lines in Fig. 4.3 locate the Brillouin frequency (6) for atoms moving in the lattice, as will be discussed in Sec. 4.3. Brillouin resonances arise from interferences between the pump and probe waves. Though their study is beyond the scope of this thesis we wish to make the following important point: The frequency-location of the Brillouin resonance depends on probe geometry but is independent of changes in the optical lattice parameters. On the other hand, the frequency-location of the vibrational frequency depends on lattice parameters, but not so much on probe geometry.

The vertical green dashed line Fig. 4.3 is drawn in between the Brillouin peak and dip - we call this the centerpoint for our x-axis, where the pump-probe detuning is zero. A feature corresponding to a slight change in slope can be discerned at the center (Rayleigh feature, see (6)), but our resolution is too weak to make any definitive statement.

Another interesting thing we studied is the dependence of the probe transmission spectrum on probe polarization (i.e., y-polarization). In the case of vertical polarization we see two resonances. We argue that due to the direction of the incident probe beam and the symmetry of the lattice the two resonances must be the vibrational resonance and the other a Brillouin resonance which arises from a distortion of the lattice due to pump-probe interference.

4.3 Experimental Data

In this section we present probe transmission spectra measured a) as a function of lattice parameter, namely the lattice intensity and detuning are varied, and b) for two different probe polarizations while the lattice stays constant. Fig. 4.5 displays the orientation of our probe beam with respect to our lattice beams. Fig. 4.6 shows measured probe spectra for a y-polarized probe traveling in the x-direction (see Fig. 3.7 for explanation of x,y,z axes) for four different lattice intensities (the intensity shown is the intensity per lattice beam; there are 4 lattice beams) while the lattice detuning was kept constant at 3.71 Γ. A dashed vertical line is drawn passing through the middle of the leftmost peak at the highest lattice intensity - recall from Sec. 4.2 that we have asserted this peak is the vibrational frequency. Another dashed vertical line is drawn through the middle of what we claim to be the Brillouin peak. We obtain three pieces of compelling evidence that support our assertions in Sec. 4.2 regarding which peak/dip in Fig. 4.3 corresponds to vibrational frequency and which corresponds to a Brillouin frequency.

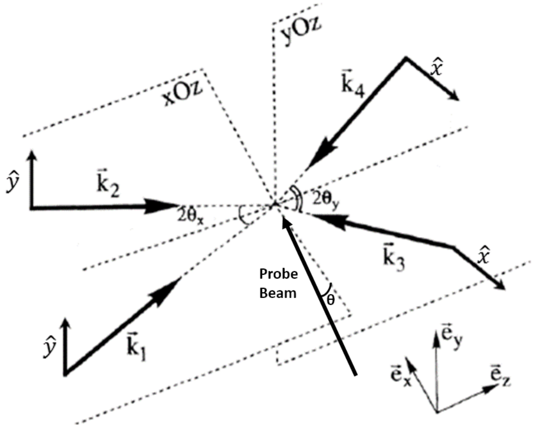

Figure 4.5: This figure displays the orientation of our probe beam with respect to our lattice beams. Our probe beam is traveling along the x-axis making a slight angle of $\theta \sim 5°$

First, it is clear from Fig. 4.6 that the leftmost peak steadily moves toward the right (i.e., frequency-location of the peak recedes toward zero) as the lattice intensity reduces at fixed lattice detuning, just as we would expect the vibrational frequency to decrease as the potential well depth decreases. On the other hand, the Brillouin peak stays put, lending credence to our assertion that this peak is a product of pump-probe interference and is unaffected by changes in the lattice.

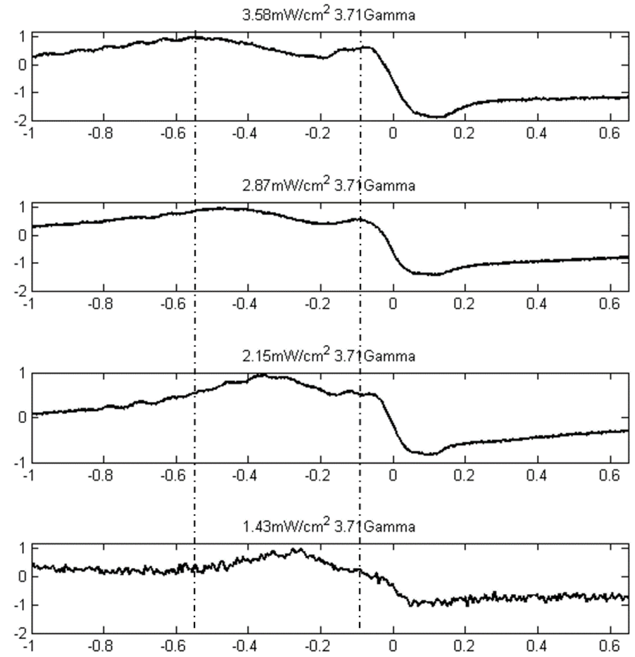

Figure 4.6: Figure displays the transmission spectra for a y-polarized probe traveling along the x-axis at various intensities (the single beam intensities are indicated).In this case the lattice and probe detuning is 3.7Γ. In this figure we draw a line through what we suspect is the Brillouin resonance to illustrate the invariance of the peak as we change the intensity of the lattice. The x-axis shows the detuning of the probe relative to the pump in MHz

Second, Fig. 4.7 shows identical spectra to Fig. 4.6 but with a z-polarized probe this time, traveling again in the x-direction. We note that because the lattice has stayed unchanged, the leftmost peak (i.e., the vibrational frequency) in Fig. 4.7 varies in a manner qualitatively similar to the vibrational frequency peak in Fig. 4.6. On the other hand, the Brillouin peak exhibits a strong dependence on probe geometry - it vanishes.

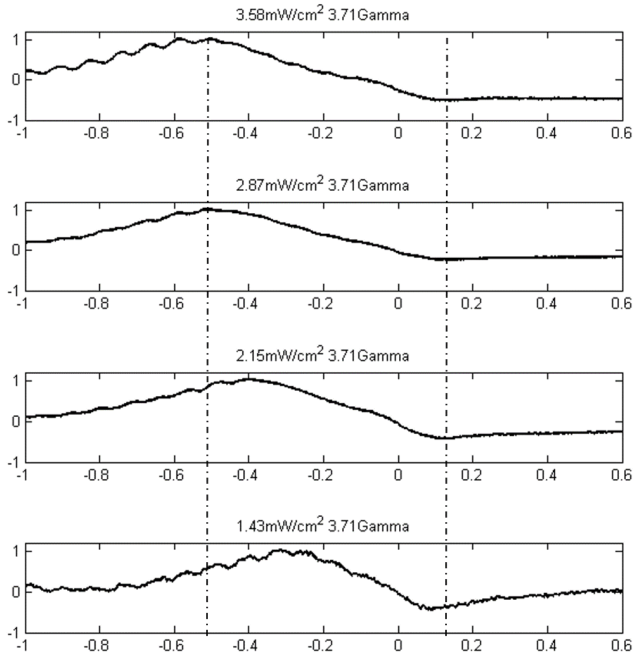

Figure 4.7: Figure displays the transmission spectra for a z-polarized probe traveling along the x-axis at various lattice beam intensities (the single beam intensities are indicated). The detuning is 3.7Γ. The x-axis shows the detuning of the probe relative to the pump in MHz

Third, measurements of the vibrational frequency for both probe polarizations are in good agreement with the theoretical estimate of vibrational frequency from Eqn. 4.1. Just like Figs. 4.6 - 4.7, Figs. 4.8 - 4.9 show probe transmission spectra of two orthogonal probe polarizations measured as a function of lattice intensity for fixed lattice detuning 5.3 Γ. Same is the case for Figs. 4.10 - 4.11, and 4.12 - 4.13 where the lattice detunings are 7 Γ and 8.6 Γ respectively. The data and theory of the vibrational frequencies from Figs. 4.6 - 4.13 are plotted in Fig. 4.14 as a function of the well-depth U_0 (expressed in units of the recoil energy E_R). In Fig. 4.14 the yellow and blue dots are the vibrational frequencies extracted from Figs. 4.6 - 4.13 for

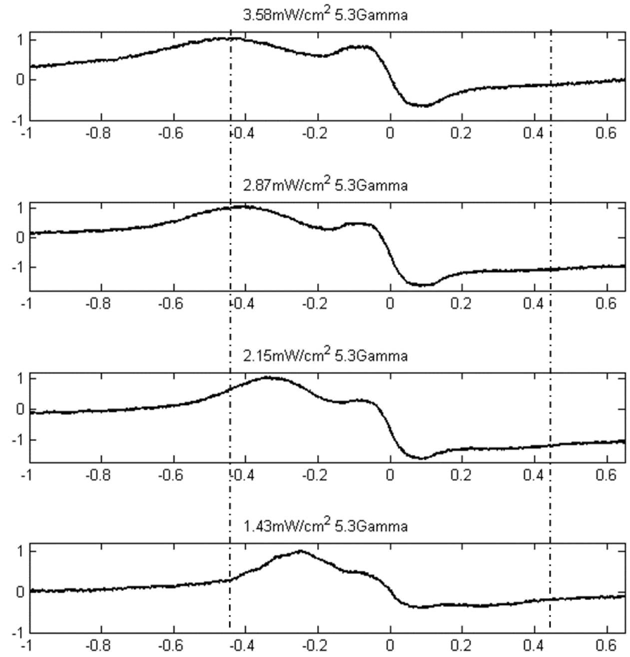

Figure 4.8: Figure displays the transmission spectra for a y-polarized probe traveling along the x-axis at various lattice beam intensities (the single beam intensities are indicated). The detuning is 5.3Γ. The x-axis shows the detuning of the probe relative to the pump in MHz

the y-polarized and z-polarized probe, respectively, propagating in the x-direction. The gray dots are the theoretical estimate from Eqn. 4.1 - the error bars reflect the uncertainty in our exact knowledge of the laser detuning - the uncertainty in our lock point which amounts to ∼ ± 1MHz. This error results in an x-error bar of ± 8 kHz (i.e., 5 U_0/E_R) and a y-error bar of 16 U_0/E_R. The error in the experimental dots (both yellow and blue) is smaller than the dot size. Clearly the theory is reasonably good agreement with the experimental data for either polarization. The orange dots represent the Brillouin frequencies for the y-polarized probe propagating in the x-direction, which appear rather insensitive to the lattice well-depth, as they should

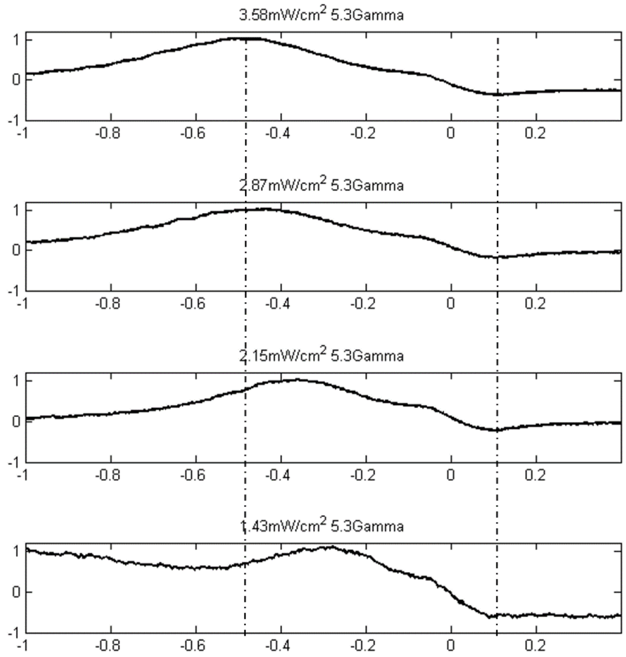

Figure 4.9: Figure displays the transmission spectra for a z-polarized probe traveling along the x-axis at various lattice beam intensities (the single beam intensities are indicated). The detuning is 5.3Γ. The x-axis shows the detuning of the probe relative to the pump in MHz

be. We conjecture that the reason the blue dots(z-polarized probe) agree better with the theoretical prediction than the yellow dots(y-polarized probe) is that the y-polarized probe interferes with the two similarly polarized lattice beams, distorting the lattice, thereby creating a Brillouin resonance observed in Figs. 4.6, 4.8, 4.10 and 4.12. On the other hand, none of the lattice beams are z-polarized, hence no interference occurs with the z-polarized probe, resulting in minimal distortion of the lattice and a highly suppressed Brillouin feature in Figs. 4.7, 4.9, 4.11 and 4.13. The theory, of course, assumes a lattice with no distortion due to pump-probe interference.

The above three evidences offer compelling support to our claim that we have

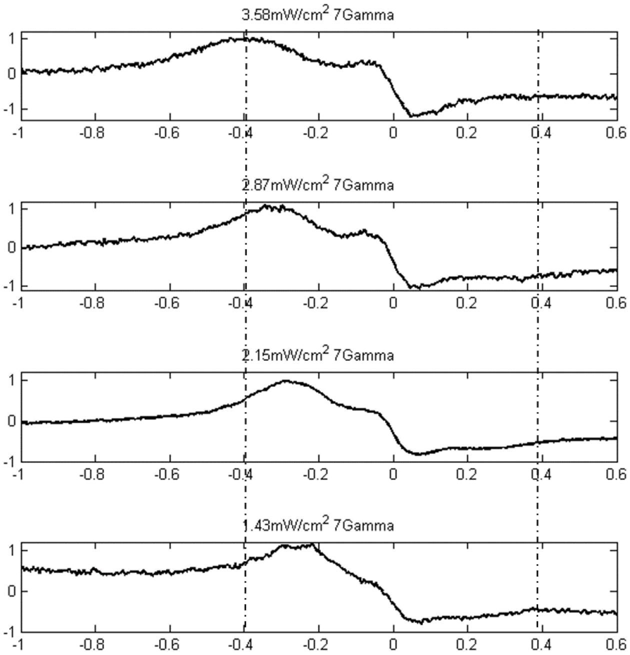

Figure 4.10: Figure displays the transmission spectra for a y-polarized probe traveling along the x-axis at various lattice beam intensities (the single beam intensities are indicated). The detuning is 7Γ. The x-axis shows the detuning of the probe relative to the pump in MHz

indeed measured the vibrational frequency for the atoms oscillating in the potential wells of our 3D optical lattice.

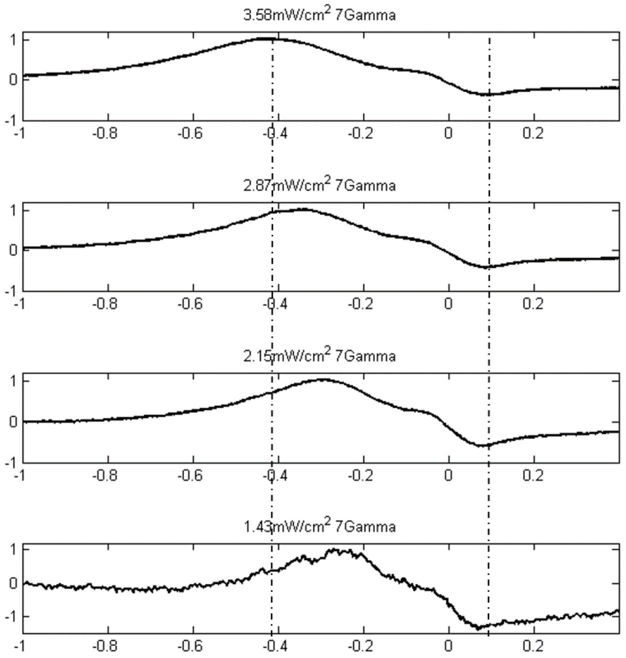

Figure 4.11: Figure displays the transmission spectra for a z-polarized probe traveling along the x-axis at various lattice beam intensities (the single beam intensities are indicated). The detuning is 7Γ. The x-axis shows the detuning of the probe relative to the pump in MHz

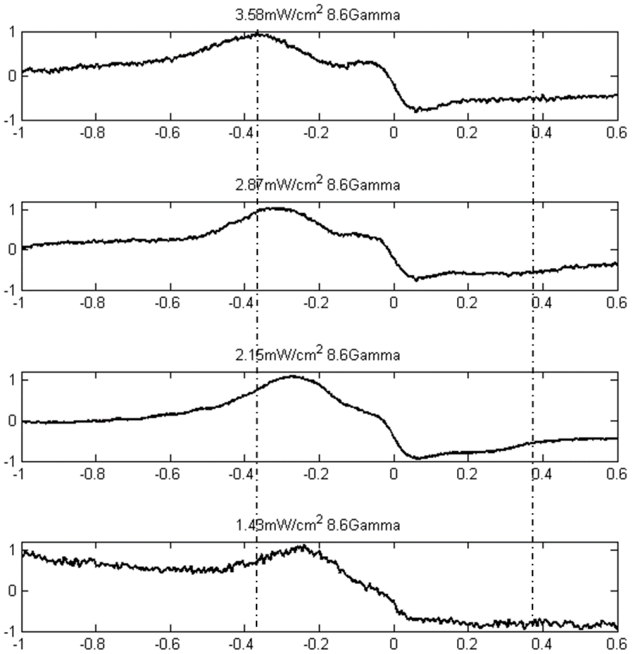

Figure 4.12: Figure displays the transmission spectra for a y-polarized probe traveling along the x-axis at various lattice beam intensities (the single beam intensities are indicated). The detuning is 8.6Γ. The x-axis shows the detuning of the probe relative to the pump in MHz

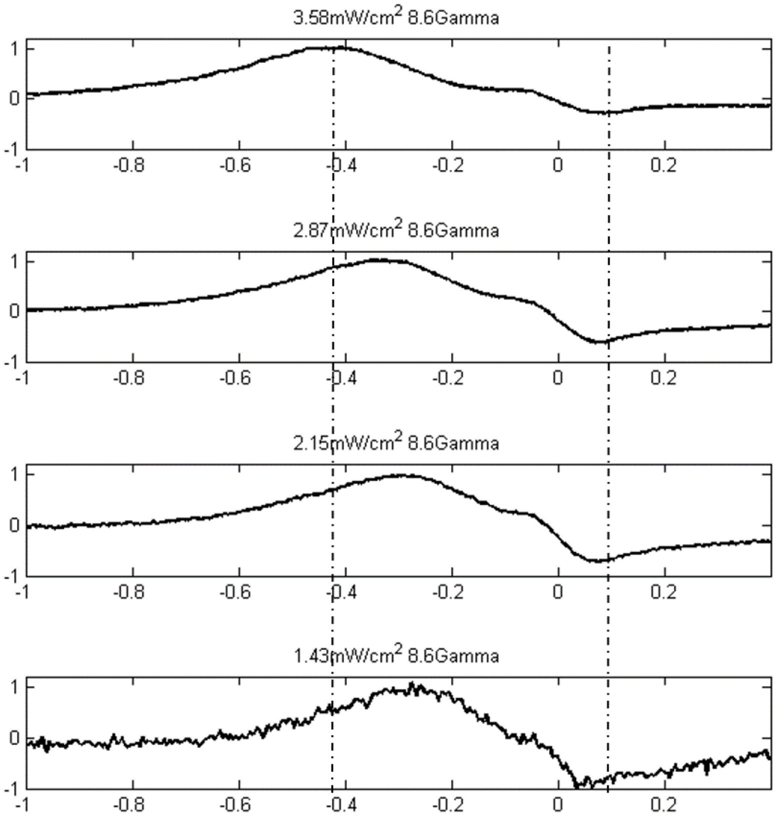

Figure 4.13: Figure displays the transmission spectra for a z-polarized probe traveling along the x-axis at various lattice beam intensities (the single beam intensities are indicated). The detuning is 8.6Γ. The x-axis shows the detuning of the probe relative to the pump in MHz

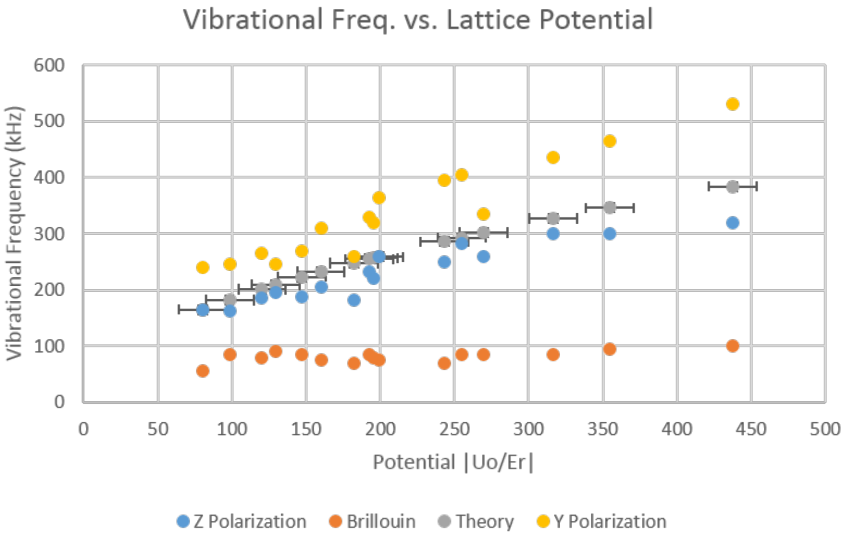

Figure 4.14: Here we see all the various frequencies extracted from Figs. 4.6-4.13 plotted against U_0/E_{Rx}. In the Graph the z-Polarization and y-Polarization correspond to which axis the probe beam is polarized along. We see good agreement to the theoretical data for the vibrational resonance in the case of both the y and z polarized probe. The z-polarized probe perturbs the lattice less since none of the lattice beams are z-polarized, hence the vibrational frequency measured by the z-probe agrees better with the theoretical prediction. See text for further explanation. For the Brillouin data we see an insensitivity to changes in the lattice well depth.

CHAPTER 5

DIGITAL INFRARED VIEWER

With the cost of high definition CCDs drastically decreasing recently there are new opportunities present to updated or redo past systems that still serve valuable purposes but still remain expensive and largely unchanged. Recently we had an idea to use easily accessible hobbyist parts to craft an inexpensive alternative to the traditional Infrared viewer. Commercial units cost $\approx$ \$2200. Using these cheap hobbyist CCDs and micro-computers and touch screen LCDs we were able to create a user friendly alternative for less than \$200.

The way infrared viewers operate is by using an image intensifier which works by focusing light onto a photo-sensitive film which releases an avalanche of electrons for every photon detected by the film. These electrons travel ballistically and are amplified, before being allowed to be incident upon a phosphorescent screen which releases a visible photon for every electron incident on it. The main cost of these viewers is the image intensifier.

Our method for creating an infrared viewer is to replace the image intensifier with a CCD array consisting of a modular Raspberry Pi camera called the PiNoIR, which connects easily to any Raspberry PI device. This inexpensive high definition camera has recently been released to hobbyists and has seen use in wildlife cameras, and imaging of flow of dye in plants. This also allows the viewer the benefit of real color comparison of the infrared light to visible light unlike the night vision green image of the traditional infrared viewer.To construct this system one requires a Raspberry

Figure 5.1: The PiNoIR camera is the component that allows us to see in the infrared. Because it is a camera that has had its infrared filter it will display images in real color and for infrared will display it as a light red or a white depending on how far it is in the infrared

Pi, the PiNoIR, a SD card, LED display/touch screen, and a battery pack. The cost of all of these components is $< \$200$ which is 10× less than the commercial model yet offers enhanced capabilities not found in the commercial model such as the ability to save images, connect to the Internet, and ability to be upgraded as time goes on. With completion and characterization of this infrared viewer we hope to explore the possibility of patenting it and also publishing a paper on its design in an instrumentation journal to make the design available to other research labs.

Much of the connection of parts is quite simple. You begin with your Raspberry Pi which is a computer that uses a processor which is utilized currently in many smartphones.This has many connection ports but the ones that we use for this purpose are the micro-USB port for power, the GPIO headers for the touch screen display, the CSI port for the PiNoIR camera, and the SD card port for the memory and operating software.

The hardware assembly for the system is quite simple and requires inserting a ribbon cable for the camera and inserting the pins into the corresponding ports for

Figure 5.2: This is a Raspberry Pi and it provides the basis for our imager. It will be the component taking the image from the camera and displaying it on a touch screen

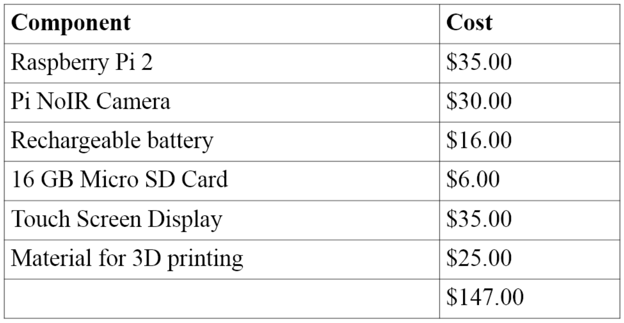

Component	Cost
Raspberry Pi 2	$35.00
Pi NoIR Camera	$30.00
Rechargeable battery	$16.00
16 GB Micro SD Card	$6.00
Touch Screen Display	$35.00
Material for 3D printing	$25.00
	$147.00

Figure 5.3: The parts lists shows the breakdown of the components needed for the infrared camera and their associated costs.

the touch screen, the memory and the battery pack. The software is a bit tricky but to start there is an open source software that you can download from Adafruit that will enable your camera and provide you with the interface to record and save your pictures. To install there is a link inserted in a how-to guide which can be followed to easily get your camera up and running. The link is https://learn.adafruit.com/diy-wifi-raspberry-pi-touch-cam/overview or can be found by searching adafruit pi camera software. One issue we ran into however was we encountered a choppiness of the image displayed. This required a bit of modification to the code in order to

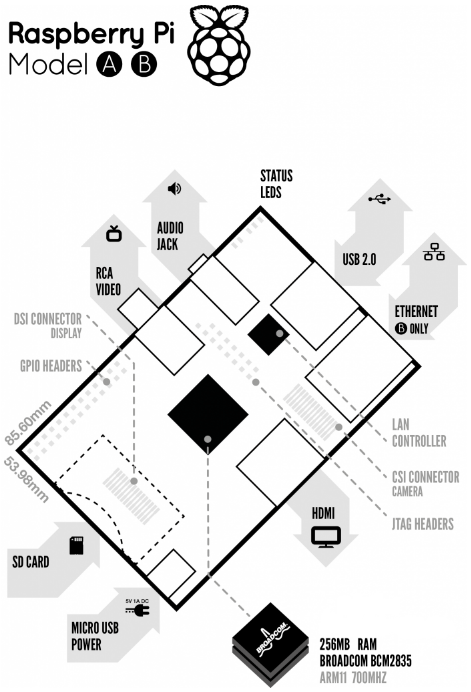

Figure 5.4: All the pins required to connect the various hardwar together is detailed in this figure

boost the frame rate. Info about increasing the framrate of the system can be found at this link http://www.pyimagesearch.com/2015/12/28/increasing-raspberry-pi-fps-with-python-and-opencv/. After making these changes we achieve a much smoother image however the frame-rate still remains a bit choppy. The slow frame-rate mostly due to the system running into limitations set by the hardware but possibly with some more masterful coding or updated hardware could be much faster. After following these directions we should be able to create a cheap alternative to the IR viewers than many use on a day to day basis in an optic lab.

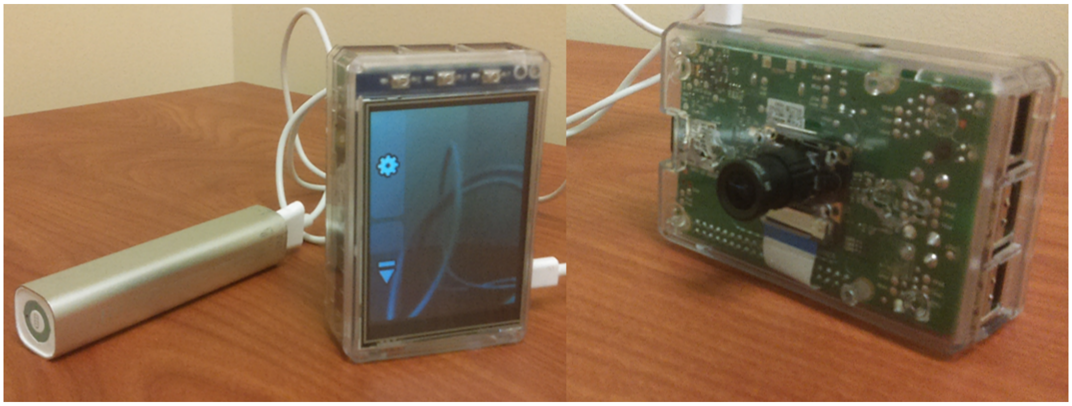

Figure 5.5: Image of the front on back of our IR viewer. We used a pre-made case and are in the process of modifying it.

CHAPTER 6

FUTURE OUTLOOK

In this chapter we describe progress made toward studying the dynamics of cold atoms in optical lattices by using a photon correlator. Studies like these have been performed before (13; 14; 15). In the future we hope to obtain data this and the other two techniques discussed. The correlator provides the link between pump-probe spectroscopy and fluorescence imaging due the correlator being able to provide diffusion constants as well as vibrational frequencies.

6.1 Optical Setup

To begin, light emitted by the atoms in the lattice is collected and collimated via a $\lambda/4$-plate through a polarizing beam splitter, as shown in Fig. 6.1. Because the atoms sit in either a σ^+ or a σ^- well we can determine based on the photon correlations we choose to observe (cross-correlation $\sigma^+ - \sigma^-$, or auto-correlation $\sigma^+ - \sigma^+$) the typical time taken by an atom to move from one well to another or, alternatively, to remain in a particular well. These two times are called the crossover time and the dwell time, respectively, and they are related to the diffusion constant (13). We are particularly interested in the first and second order correlations given by (13; 14; 15).

$$g_1^{\sigma^+-\sigma^+}(\tau) = \frac{\langle E_{\sigma^+}(t)E_{\sigma^+}(t+\tau)\rangle}{\langle I_{\sigma^+}(t)\rangle}, g_2^{\sigma^+-\sigma^+}(\tau) = \frac{\langle I_{\sigma^+}(\tau)I_{\sigma^+}(t+\tau)\rangle}{\langle I_{\sigma^+}(t)\rangle^2} = 1 + |g_1^{\sigma^+-\sigma^+}(\tau)|^2 \tag{6.1a}$$

$$g_1^{\sigma^+-\sigma^-}(\tau) = \frac{\langle E_{\sigma^+}(t)E_{\sigma^-}(t+\tau)\rangle}{\langle I_{\sigma^+}(t)\rangle}, g_2^{\sigma^+-\sigma^-}(\tau) = \frac{\langle I_{\sigma^+}(\tau)I_{\sigma^-}(t+\tau)\rangle}{\langle I_{\sigma^+}(t)\rangle^2} \tag{6.1b}$$

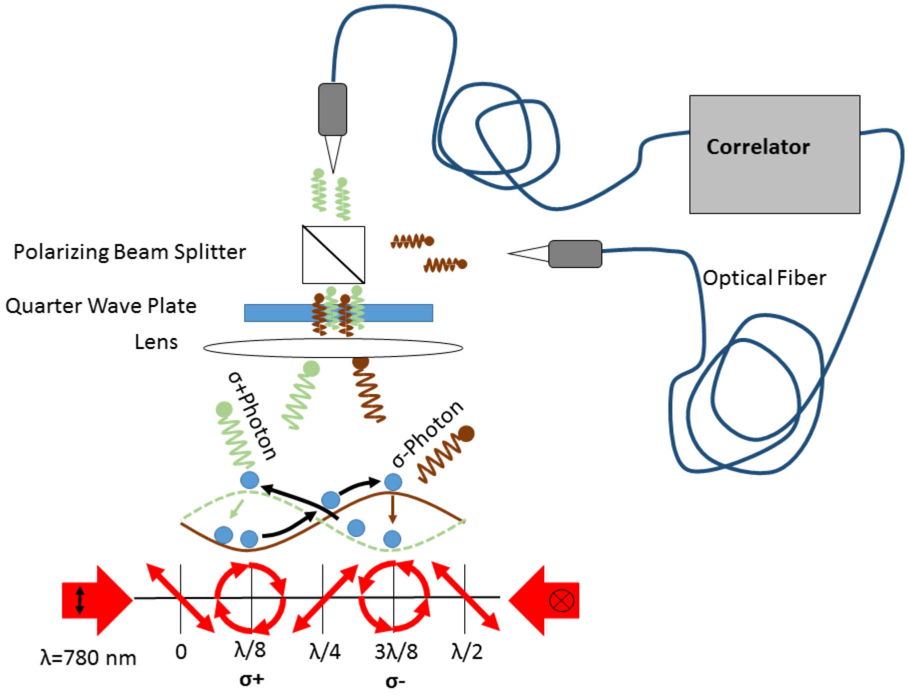

Figure 6.1: This is the setup that is required to do intensity correlation measurements. The lens collects the photons and focuses them through a quarter wave plate converting them into orthogonal linear polarizations symbolized by the red and green color. These then enter photo-detectors where the photons are timestamped and any correlations are determined

$$= 1 + |g_1^{\sigma^+ - \sigma^-}(\tau)|^2 \propto e^{-2\delta k^2 D\tau} \tag{6.1c}$$

where τ is the time step between photon events, δk = k(1-cosθ) which is the difference between the z components of the wave vectors of the scattered field (13). $E_{\sigma^\pm}$ is the electric field incident on the $\sigma^\pm$ detector, and $I(t)$ is the intensity.

6.2 Photon Correlator

To measure the cross-over time given by $g_2^{\sigma^+ - \sigma^-}$, the output from the σ^+ detector is time-stamped and then compared with the future counts from the σ^- detector. To measure the dwell-time given by $g_2^{\sigma^+ - \sigma^+}$, the time stamp of one event from the the σ^+ detector is compared to the future time stamps of the same detector. The diffusion constant D can be found by using the proportionality of $g_2(\tau)$ to the exponential given in Eqn. 5.1(c) (13). This relationship is what we will use to test the photon correlation method against the methods of fluorescence imaging(Chap. 3) and pump-probe spectroscopy(Chap. 4). By using sensitive single photon counters we can time-stamp when single-photon events happen and measure the correlation between photons of the same polarization (dwell time) or different polarizations (cross-over time).

To build such a correlator we followed a guide for a correlator made by Joffrey Peters et. al. at NIST (16). The correlator consists of a FPGA which timestamps the arrival of a photon. We then run this series of timestamps back through to determine if there is a correlation between photons arriving at a specified time interval. In Fig. 6.3 we describe the characteristics of the photon correlator described in the guide provided by Migdall's group at NIST.

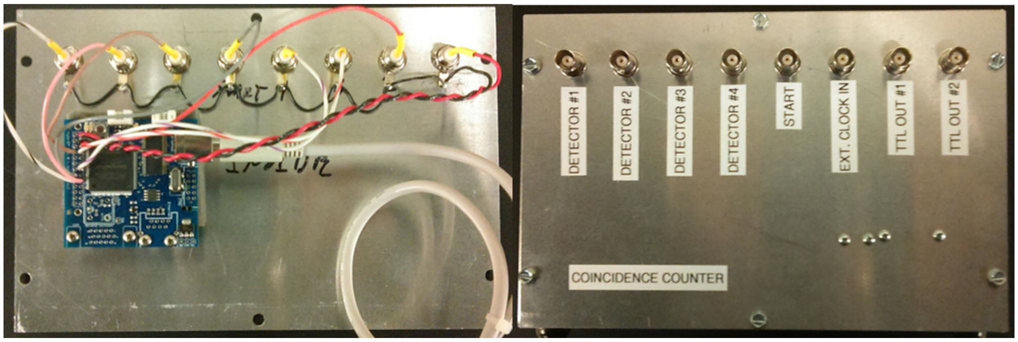

Figure 6.2: This is the photon correlator recently constructed and consists of only BNC ports and a Field Programmable Gate Array (FPGA). This is what we will use to perform correlations on the photons emitted by atoms as they move through the lattice.

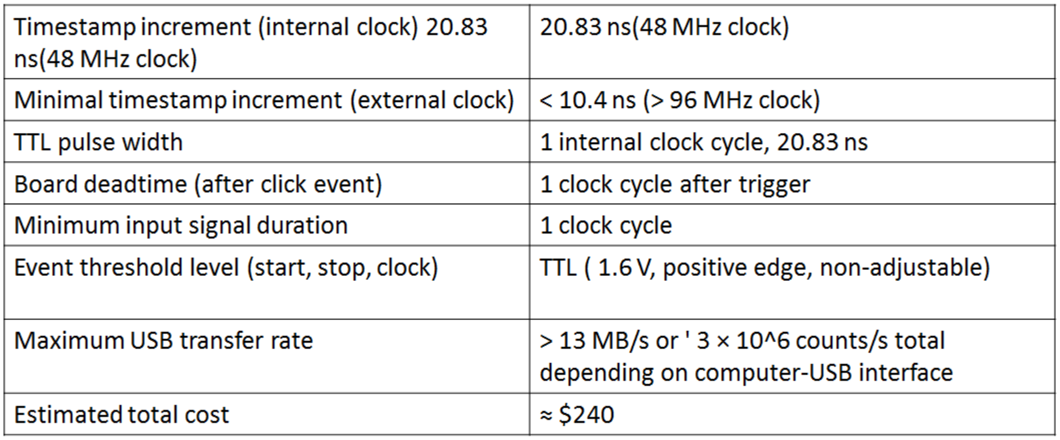

Timestamp increment (internal clock) 20.83 ns(48 MHz clock)	20.83 ns(48 MHz clock)
Minimal timestamp increment (external clock)	< 10.4 ns (> 96 MHz clock)
TTL pulse width	1 internal clock cycle, 20.83 ns
Board deadtime (after click event)	1 clock cycle after trigger
Minimum input signal duration	1 clock cycle
Event threshold level (start, stop, clock)	TTL (1.6 V, positive edge, non-adjustable)
Maximum USB transfer rate	> 13 MB/s or ' 3 × 10^6 counts/s total depending on computer-USB interface
Estimated total cost	≈ $240

Figure 6.3: This table outlines the characteristics of the photon correlator. These characteristics were given in Ref.[17] and have yet to be tested by us for our unit.

6.3 Working With FPGA Time Tagger

All the necessary software and firmware can be downloaded from NIST's website (”Simple and Inexpensive FPGA-based Fast Multichannel Acquisition Board”). Of the two provided LabVIEW programs, Coincidence Counter and TimeTag, we require only the TimeTag program as this actively time-stamps detected pulses and allows for post-analysis, whereas the counter only records the number of counts and coincidences for each channel.

Before running either VI, it's important to have configured the FPGA first. There is a program, FPGAConfig, from which the FPGA can be configured by selecting the appropriate program from a drop-down menu. Once this is done, the TimeTag program can be run.

The program has an active display showing individual counts and coincidences between channels. It saves the data at a location inputted by the user, and each data point (coincidence between two or more channels) is recorded in binary as 4 bytes in little endian format, with each bit's information tabulated in the manual. It is important to note that the program automatically saves the data in binary, not pseudo-binary as the manual suggests. A binary viewer (we use one from ProXoft) can ultimately confirm the format of the outputted data.

At this point, the raw data can be analyzed afterwards with MATLAB.

6.4 Data Analysis Code

After obtaining the data file output from the FPGA some basic sorting needed to be done with the data in order to easily analyze the data and obtain the auto and cross correlation spectra.

The timetag box has 4 channels (see Fig.6.4) that can all record photon "clicks". However for our uses we only care about using two channels. In order to prevent accidental clicks from noise on the unused channels 50Ω terminators are attached. The counts that are recorded are stored as a timetag value which corresponds to the clock cycle that the FPGA was on when the click occurred, a 1 or 0 in the corresponding channel column depending on if a click was measured in that channel, and a 1 or 0 in the reset channel which signifies if the clock counter is reseting due to the finite size of the clock counter.

Table 8: Raw Timetagged Data Format

Bit:	26-0	27	28	29	30	31
Meaning:	Timestamp	Ch. 1	Ch. 2	Ch. 3	Ch. 4	Counter cleared

Figure 6.4: The time tag string that is recieved is comprised of these 6 bit sections. 26-0 are the actual time tag. If 27, 28, 29,30 are one they received a signal during that time tag. If 31 is 1 the clock reach its max value and reset.

The data that was output begins in ASCII and is converted to 8 bit binary strings. One timetag consists of 4 8-bit strings that must be swapped around to obtain the time stamp, the channel counts, and the reset signal for the clock counter.

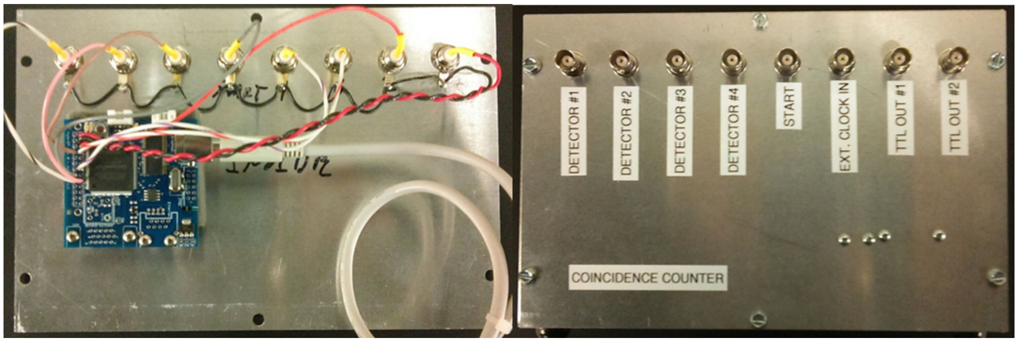

Figure 6.5: This is the photon correlator recently constructed and consists of only bnc ports and a Field Programmable Gate Array (FPGA). This is what we will use to perform correlations on the photons emitted by atoms as they move through the lattice.

CHAPTER 7

CONCLUSION

In conclusion we have presented our study of 1-D and 3-D optical lattices in which we measured diffusion constants with fluorescence imaging and vibrational resonances with pump-probe spectroscopy. Our future outlook to compare our diffusion constants and vibrational resonances directly using photon correlation methods.

With diffusion constants we see agreement to with-in an order of magnitude with prior work done by Schiavoni (6). We also see clear trends in the value of the diffusion constant when varying the lattice detuning while holding the lattice intensity constant and vice versa. This gives us confirmation that our imaging system is providing logical results and can be used to further explore atomic dynamics in optical lattices

In pump-probe spectroscopy we see interesting features in our probe spectra as we scan our pump and believe we have accurately identified both vibrational and Brillouin resonances. We have some slight indication of Rayleigh resonances but these lack proper resolution and require a much finer exploration. In our spectra our vibrational resonances show distinct dependence on intensity and detuning and an independence on probe geometry. In our Brillouin resonances we see an independence from intensity and detuning while also seeing a very clear dependence on probe geometry. When plotting these values against a theoretical model detailed in Ref. (10) we see close agreement with what they predict. This understanding opens the door to study further the fine structure of optical lattices.

With our new understanding of atomic diffusion and vibrational resonances we should soon be able to perform a study on the relation between the vibrational resonances and diffusion constant upon the completion of our correlation setup. We have implemented the hardware required to perform the spectroscopy but work is still necessary to be able to confidently analyze the data supplied by the time tagger. With completion and calibration of our correlation setup we should be able to connect diffusion constants and vibrational resonances together using the correlation measurements. We will also be able to study the dwell time and cross over time of atoms interacting with the optical lattice.(13)

Overall we now have a grasp on our fluorescence imaging setups and pump-probe spectroscopy setups opening the door to many future studies of optical lattices and ratchets.

Appendix A

APPENDIX A

In the past year I had the privilege of disassembling a crystal and I gained some insight on the inner workings of an AOM. First note to give to any future students who are for some reason tasked with opening one up is that **the two screws on the bottom of the modulator are set screws for the crystal and should not be removed unless you have self destructive tendencies**. The screw you are looking for is on top of the modulator conveniently hidden below the manufacturers label. There is a perforated circle on the label that can be peeled back using a razor blade revealing the screw. The internal components look like the following.

Appendix B

APPENDIX B

```
function FWHM()

clear;
%This function is used to analyze the data collected from the pump-probe
%runs.  Contributors are Ethan Clements, Anthony Rapp, and assistance from
%Preston Ross

%Set a tolerance for the data. Gives a width around the
expected value of the half max. Because of descritation
of points that specific value may not exist. This is used
to average over a small section of data to find the central
point which is very close to the half max.
tolerance = 200;

%First select the directory of the files be assesed here
theDir = uigetdir('Please Select a Directory Of Data Files');
cd(theDir);
files = dir('*.txt'); %load all txt files
%Place all of the data into one large cell array
```

```
for i=1:length(files)
TempCell{i} = load([files(i).name],theDir);
end

%Take every part of that cell array and turn it into a workable variable
%that we can use
image = cat(3,TempCell{1:end});

%Pick the respective background file (created earlier)
%UI comes up to select a folder where the background is
BackDir = uigetdir('Select the directory with the background files');
cd(BackDir);
load('AverageBackground.mat');

%Switch back to old directory for purposes of saving
cd(theDir);

[m,n,p] = size(image);
DataArray = zeros(p,1);

for i=1:p
%Sometimes a data point is bad enough that it
goes out of the bounds of
%the program and crashes it. Keep in the disply
so that when it
%crashes, we can see exactly which file crashed
it, and remove that
%data point
```

```
disp(i)
BackSub = image(1:end,1:end,i) - background;
%imported file - background image
%The edge is a 0 and drop off, better to just remove it
BackSub = BackSub(2:end,1:end);
surf(BackSub)

%N = length(image);
xArray = 1:length(BackSub); %create a row from 1 to 125

SumIY = sum(sum(BackSub)); %scalar sum of all intensity values

c = xArray*BackSub;
%disp(c)
SumY = sum(c); %scalar for weighted values
%disp(SumY)
%disp(SumIY)
CoMY = SumY/SumIY;
XSecond = (BackSub)'; %transpose image

SumIX = sum(sum(XSecond));
d = xArray*XSecond;
SumX = sum(d); %scalar for weighted values
CoMX = abs(SumX/SumIX);
%disp(['CoMX = ',num2str(CoMX)]);
%disp(['CoMY = ',num2str(CoMY)]);
XMiddle = BackSub(round(CoMY),:);
%extract Y row located at CoMY
```

```
YMiddle = BackSub(:, round(CoMX));
%extract X column located at CoMX
MAXINT = BackSub(round(CoMY),round(CoMX));
%disp(['MAXINT = ',num2str(MAXINT)]);
MINArray = BackSub(1:20,1:20);
MINAVG = mean(mean(MINArray));
%disp(['MINAVG = ',num2str(MINAVG)]);
HalfMAX = ((MAXINT-MINAVG)/2)+MINAVG;
%disp(['HalfMAX = ',num2str(HalfMAX)]);

%disp(BoundsX)
%disp(BoundsY)

BoundL = XMiddle(1:(round(CoMX)));
BoundR = XMiddle(round(CoMX):length(XMiddle));
BoundU = YMiddle(1:(round(CoMY)));
BoundD = YMiddle(round(CoMY):length(YMiddle));
BoundXL = find(BoundL>(round(HalfMAX)-tolerance)
& BoundL<(round(HalfMAX)+tolerance));
BoundXR = find(BoundR>(round(HalfMAX)-tolerance)
& BoundR<(round(HalfMAX)+tolerance));
BoundYL = find(BoundU>(round(HalfMAX)-tolerance)
& BoundU<(round(HalfMAX)+tolerance));
BoundYR = find(BoundD>(round(HalfMAX)-tolerance)
& BoundD<(round(HalfMAX)+tolerance));
%disp(BoundL);
%disp(BoundR);
%disp(BoundU);
```

```
%disp(BoundD);
LFWHM = mean(BoundXL);
RFWHM = mean(BoundXR)+CoMX;
UFWHM = mean(BoundYL);
DFWHM = mean(BoundYR)+CoMY;
YFWHM = RFWHM - LFWHM;
XFWHM = DFWHM - UFWHM;
%disp(['YFWHM = ',num2str(YFWHM)])
%disp(['XFWHM = ',num2str(XFWHM)])
%surf(BackSub)
DataArray(i,1) = XFWHM;
DataArray(i,2) = YFWHM;
end


%This first portion saves just the data array, consisting of all of the
%full-width half-max values of both x(1) and y(2).
save('DataArray.mat','DataArray');

disp('Finished!');
```

BIBLIOGRAPHY

[1] Lewenstein et. al. Ultracold atomic gases in optical lattices: Mimicking condensed matter physics and beyond", advances in physic. *Advances in Physics*, 56(1):243–379, 2007.

[2] E. Lutz et. al. Beyond boltzmann-gibbs statistical mechanics in optical lattices. *Nature Physics*, 9(1):615–619, 2013.

[3] Y. Sagi et. al. Observation of anomalous diffusion and fractional self-similarity in one dimension. *Physical Review Letters*, 108(1):108, 2012.

[4] K. B. MacAdam et. al. A narrow-band tunable diode laser system with grating feedback, and a saturated absorption spectrometer with cs and rb. *American Journal of Physics*, 60(12):1098–1111, 1992.

[5] J. Kangara et. al. Design and construction of cost-effective fail-safe tapered amplifier systems for laser cooling and trapping experiments. *American Journal of Physics*, 82(8):805–817, 2014.

[6] M. Schiavoni. Atomic dynamics in a dissipative optical lattice: Propagation modes, stochastic resonances, directed diffusion. *PhD thesis, National University Kastler Brossel Laboratory*, 2003.

[7] A. J. Hachtel et. al. Note: Design and implementation of a home-built imaging system with low jitter for cold atom experiments. *Review of Scientific Instruments*, 87(1):1–3, 2016.

[8] P. Jessen. An investigation of the microscopic motion of atoms in optical molasses using optical heterodyne spectroscopy of resonance fluorescence. *PhD thesis, University of Aarhus, Denmark*, 1993.

[9] T. W. Hodapp et. al. Three-dimensional spatial diffusion in optical molasses. *Applied Physics B*, 60(1):135–143, 1995.

[10] K. I. Petsas et. al. Crystallography of optical lattices. *Physical Review A*, 50:5173–5189, 1994.

[11] N. Souther et. al. Measurements of light shifts in cold atoms using raman pump-probe spectroscopy. *Laser Physics Letters*, 7(4):321–327, 2010.

[12] G. Grynberg et. al. Cold atoms in dissipative optical lattices. *Physics Reports*, 355(1):335–451, 2001.

[13] C Jurczak et. al. Atomic transport in an optical lattice: An investigation through polarization- selective intensity correlations. *Physical Review Letters*, 77(9):1727–1730, 1996.

[14] S. Bali et. al. Measurement of intensity correlations of scattered light from optically-trapped atoms. *Physical Review A*, 53:3469–3472, 1995.

[15] R. Stites et. al. Sensitive measurement of radiation trapping in cold atom clouds by intensity correlation detection. *Optics Letters*, 29:2713–2715, 2004.

[16] J. Peters et. al. Simple and inexpensive fpga-based fast multichannel acquisition board.